



Nanobodies to multiple spike variants and inhalation of nanobody-containing aerosols neutralize SARS-CoV-2 in cell culture and hamsters

Metin Aksu^{a,1}, Priya Kumar^{b,1}, Thomas Güttler^{a,c}, Waltraud Taxer^a, Kathrin Gregor^a,
 Bianka Mußil^a, Oleh Rymarenko^a, Kim M. Stegmann^b, Antje Dickmanns^b, Sabrina Gerber^b,
 Wencke Reineking^d, Claudia Schulz^e, Timo Henneck^{e,f}, Ahmed Mohamed^{e,f},
 Gerhard Pohlmann^g, Mehmet Ramazanoglu^g, Kemal Mese^h, Uwe Groß^h, Tamar Ben-Yedidiaⁱ,
 Oded Ovadiaⁱ, Dalit Weinstein Fischerⁱ, Merav Kamenskyⁱ, Amir Reichmanⁱ,
 Wolfgang Baumgärtner^d, Maren von Köckritz-Blickwede^{e,f}, Matthias Dobbstein^{a,b,*},
 Dirk Görlich^{a,**}

^a Max Planck Institute for Multidisciplinary Sciences, Dept. of Cellular Logistics, Am Fassberg 11, 37077 Göttingen, Germany

^b University Medical Center Göttingen, Dept. of Molecular Oncology, Justus von Liebig Weg 11, 37077 Göttingen, Germany

^c Octapharma Biopharmaceuticals GmbH, Im Neuenheimer Feld 590, 69120 Heidelberg, Germany

^d Department of Pathology, University of Veterinary Medicine Hannover, Bünteweg 17, 30559 Hannover, Germany

^e Research Center for Emerging Infections and Zoonosis (RIZ), University of Veterinary Medicine Hannover, Bünteweg 17, 30559 Hannover, Germany

^f Department of Biochemistry, University of Veterinary Medicine Hannover, Bünteweg 17, 30559 Hannover, Germany

^g Fraunhofer Institute for Toxicology and Experimental Medicine ITEM, Nikolai-Fuchs Str. 1, 30625 Hannover, Germany

^h University Medical Center Göttingen, Dept. of Medical Microbiology and Virology, Kreuzberggring 57, 37075 Göttingen, Germany

ⁱ Scinai Immunotherapeutics Ltd., Jerusalem BioPark, Hadassah Ein Kerem, Jerusalem, 9112001, Israel

ARTICLE INFO

Keywords:

SARS-CoV-2
 Variants of concern
 Spike
 Receptor binding domain
 Nanobodies
 VHH antibodies
 Protein structure
 Inhalation
 Aerosol
 COVID-19
 Animal model
 Hamster

ABSTRACT

The ongoing threat of COVID-19 has highlighted the need for effective prophylaxis and convenient therapies, especially for outpatient settings. We have previously developed highly potent single-domain (VHH) antibodies, also known as nanobodies, that target the Receptor Binding Domain (RBD) of the SARS-CoV-2 Spike protein and neutralize the Wuhan strain of the virus. In this study, we present a new generation of anti-RBD nanobodies with superior properties. The primary representative of this group, Re32D03, neutralizes Alpha to Delta as well as Omicron BA.2.75; other members neutralize, in addition, Omicron BA.1, BA.2, BA.4/5, and XBB.1. Crystal structures of RBD-nanobody complexes reveal how ACE2-binding is blocked and also explain the nanobodies' tolerance to immune escape mutations. Through the cryo-EM structure of the Ma16B06-BA.1 Spike complex, we demonstrated how a single nanobody molecule can neutralize a trimeric spike. We also describe a method for large-scale production of these nanobodies in *Pichia pastoris*, and for formulating them into aerosols. Exposing hamsters to these aerosols, before or even 24 h after infection with SARS-CoV-2, significantly reduced virus load, weight loss and pathogenicity. These results show the potential of aerosolized nanobodies for prophylaxis and therapy of coronavirus infections.

1. Introduction

Coronavirus-induced disease (COVID-19), caused by Severe Acute

Respiratory Syndrome Coronavirus 2 (SARS-CoV-2), continues to represent a major threat to public health, especially when taking the potential of future variants into account. While available vaccines can

* Corresponding author. University Medical Center Göttingen, Dept. of Molecular Oncology, Justus von Liebig Weg 11, 37077, Göttingen, Germany.

** Corresponding author.

E-mail addresses: mdobbstein@uni-goettingen.de (M. Dobbstein), goerlich@mpinat.mpg.de (D. Görlich).

¹ Equal first authors.

reduce the severity of the disease, they do not prevent it entirely, and long-term effects such as Long COVID remain a major health concern. Furthermore, currently available therapies, such as the protease-inhibiting Nirmatrelvir, offer limited solutions to the problem (Jami-son et al., 2022; Murakami et al., 2023). Although avoiding exposure to the virus through measures such as mask-wearing and social distancing is possible, it is often difficult to maintain in practice. Therefore, a prophylactic option would be highly desirable to avoid the disease in the event of accidental exposure to the virus, especially for at-risk populations. Such prophylaxis would need to be readily available and easily applicable.

SARS-CoV-2 entry into host cells is mediated by trimeric spikes on the surface of viral particles (Li et al., 2003). It is initiated by docking of the receptor binding domain (RBD) of the Spike to its host receptor ACE2 (angiotensin-converting enzyme 2). Structural rearrangements of the Spike then trigger fusion of the viral membrane with a host cell membrane. The Spike can present its RBDs in either an “up” or a “down” conformation, but only an up RBD is compatible with ACE2 binding. Accordingly, many neutralizing antibodies bind an RBD in the up conformation and compete with ACE2-binding to block viral infection.

Monoclonal antibodies against the Spike protein of SARS-CoV-2 have been used for virus neutralization in a therapeutic setting (Chen et al., 2022). Typically, these antibodies were administered to COVID-19 patients by intravenous infusion. Despite their therapeutic benefit, they come with limitations. These include high costs and poor availability due to insufficient production scale. Moreover, virus variants have developed resistance against the most of these antibodies (Cox et al., 2023). Finally, intravenous infusion requires a trained professional for performing the phlebotomy. These drawbacks raise the need for effective, easy-to-use alternatives.

We (Güttler et al., 2021) and others (Custódio et al., 2020; Huo et al., 2021; Koenig et al., 2021b; Maeda et al., 2022; Mast et al., 2021; Pymm et al., 2021; Rossotti et al., 2022; Sasisekharan, 2021; Xiang et al., 2020, 2022; Xu et al., 2021; Ye et al., 2021) have previously reported the development of VHH antibodies, also known as nanobodies, for SARS-CoV-2 neutralization. Nanobodies correspond to the antigen-binding domains of heavy chain-only antibodies found in camelids (Arbabi Ghahroudi et al., 1997; Hamers-Casterman et al., 1993). For this project, alpacas were immunized with the Spike protein or with RBD fusions, followed by blood sampling, and isolation of lymphocytes and subsequently of RNA. VHH coding regions were reverse-transcribed, PCR-amplified and cloned into a phagemid, followed by phage display selection of the strongest binders to Spike and the RBD. Advantages of nanobodies over conventional immunoglobulins include that large immune libraries can be constructed without the complication of light-heavy-chain-combinatorics. This makes it easier to select binders with high affinity. Furthermore, the simpler fold allows for binders with extraordinary thermostability and long shelf life as well as their production in inexpensive systems like bacteria or yeast. The first generation of nanobodies we obtained in this way was capable of neutralizing the virus in low picomolar concentrations (Güttler et al., 2021), and this was reflected by large interfaces, as observed in the X-ray crystal structure of the nanobodies in complex with the RBD of the Spike.

This first generation of nanobodies was developed to neutralize the Wuhan strain and early variants of SARS-CoV-2. However, a large body of virus variants has emerged since then, and some of these variants became dominant in certain areas and periods. Currently, Omicron and its subvariants are most prevalent. The variants contain multiple exchanges of amino acid residues within the Spike, in particular at the RBD, where neutralizing antibodies typically bind. Correspondingly, most antibodies that were developed against the original strain fail to neutralize Omicron (Moulana et al., 2023; VanBlargan et al., 2022), and the same turned out for our first generation nanobodies. However, some studies found that the generation of broadly active nanobodies that cover Omicron variants is not impossible (Maeda et al., 2022; Xiang et al., 2022).

To render nanobodies useful in COVID-19 prophylaxis and therapy, we now aimed at two improvements. Firstly, we developed a new generation of nanobodies that can neutralize more recent variants of SARS-CoV-2 as broadly as possible, binding to the variant RBDs with high affinity and in a mutation-tolerant manner. Structural analyses explained these features. These nanobodies not only require identification and characterization, but also the development of manufacturing processes for efficient production on a large scale, meeting the requirements of Good Manufacturing Practice (GMP) to become suitable for clinical use.

Secondly, we were aiming at a convenient application that diminishes the deleterious contact between the virus and its first target cells as early as possible, just when the virus reaches the mucosa. This is possible by inhalation of nanobodies, delivering them directly to the site of infection. Previous studies suggest that inhalation might represent an effective administration route for conventional antibodies (Piepenbrink et al., 2021) or an ACE2-decoy (Zhang et al., 2022) and even more so for nanobodies (Gai et al., 2021; Nambulli et al., 2021; Van Heeke et al., 2017; Wu et al., 2022; Xiang et al., 2022) against SARS-CoV-2. However, delivery of proteins by such a route remains challenging and requires a specific formulation to reach both upper and lower airways of the entire lung (Ari and Fink, 2020; Dolovich and Dhand, 2011; Hickey and Stewart, 2022; Longest et al., 2019; Mayor et al., 2021). In particular, the question remains whether nanobody inhalation might not only prevent the infection in a prophylactic setting, but whether it also ameliorates the disease when applied to pre-infected respiratory epithelia. So far, the most far-reaching ‘therapeutic’ setting reported was nanobody inhalation 6 h post infection (Nambulli et al., 2021), but treating a truly established SARS-CoV-2 infection with inhaled nanobodies has not been attempted yet. We now subjected nanobodies to nebulization in small droplets. When hamsters were exposed to these aerosols, they became almost completely resistant to SARS-CoV-2 in a prophylactic setting. Even when the aerosols were only applied as late as 24 h after infection, we still observed a substantially diminished virus load and less pronounced weight loss of animals. This argues that inhaled nanobodies are not only protective against the virus but even ameliorate established infections.

2. Results

2.1. Next generation nanobodies display high affinity to spike proteins from SARS-CoV-2 variants, including Omicron

In previous work (Güttler et al., 2021), VHH antibodies from three alpacas immunized with SARS-CoV-2 S1 and RBD were obtained, including neutralizing VHH antibodies directed against two RBD epitopes, namely epitope 1 (the main epitope defined by VHH antibody Re5D06) and epitope 2 (the epitope defined by the VHH antibody Re9F06). Epitope 1 has a very large overlap with the ACE2 interface, epitope 2 only a small overlap. Epitope 1-binders such as Re5D06 were found to be more potent in neutralization (neutralizing down to concentrations of 50 pM) than epitope 2-binders (so far not better than 1.7 nM). However, epitope 1 was found to be mutated in all initial variants of concern (VOC), namely in Alpha (N501Y), Beta (N501Y, E484K, K417N), Gamma (N501Y, E484K, K417T), Delta (L452R, T478K), Epsilon (L452R) and Mu (E484K, N501Y). These escape mutations impede binding and neutralization by epitope 1-binding VHH antibodies, then rendering them ineffective in therapeutic applications.

As a solution to the problem, we repeatedly re-immunized the same three alpacas with wildtype and mutant spike proteins, allowing further affinity maturation of antibodies and their adaptation to RBD mutations. Immune libraries were prepared, and phage display was performed, cross-selecting with alternating RBD versions as a bait, namely with a “wildtype” RBD corresponding to the original Wuhan strain and a “tetramutant” RBD that combines the four key immune escape mutations K417T, L452R, E484K, and N501Y found in the Alpha, Beta, Gamma,

Delta, Epsilon and Mu SARS-CoV-2 strains. The phage display also comprised a selection against non-neutralizing VHH-antibodies, using an RBD-ACE2 fusion as a competitor against VHHs that do not block the RBD-ACE2 interaction.

This combined strategy yielded new VHH antibodies. These include VHH variants of previously isolated classes, e.g., belonging to the Re9B09 class (Güttler et al., 2021), mostly however, new VHH sequences, notably Re30H02 and the Re32D03 class comprising Re32D03, Re32B11, and Ma6F06 (Fig. 1A; Suppl. Fig. 1). When analyzed by bio-layer interferometry (Abdiche et al., 2008), these VHHs showed extreme affinities (with almost no detectable dissociation) towards immobilized RBDs of the Wuhan as well as Beta, Gamma and Delta variants of SARS-CoV-2 (Fig. 1B).

The SARS-CoV-2 VOC Omicron (B.1.1.529, now called BA.1) is a remarkable variant, harboring more than 30 escape mutations in the SARS-CoV-2 Spike protein alone. Fifteen of these, namely G339D, S371L, S373P, S375F, K417N, N440K, G446S, S477N, T478K, E484A, Q493R, G496S, Q498R, N501Y, and Y505H, are in the RBD domain.

Unlike the earlier VOCs, these escape mutations reside not only in epitope 1 but also in epitope 2, hampering the binding abilities of most of the selected VHH antibodies, including Re32D03 class members (Fig. 2A), hence limiting their effectiveness in virus neutralization. The Omicron variant has later diverged to >300 subvariants, notable ones being BA.2, BA.2.75, BA.4, BA.5, BQ.1, and XBB.1. Overall, the Omicron set of variants of SARS-CoV-2 is particularly challenging as an immunogen. In addition to Omicron Spike proteins deviating from the Wuhan strain to a much greater extent than the Alpha through Delta variants, Omicron variants also give rise to less strongly binding antibodies when compared with the original virus Spike in immunization experiments (He et al., 2022).

Nonetheless, we attempted to generate nanobodies that bind and neutralize Omicron variants. We re-immunized Xenia, the alpaca that gave rise to Re32D03 class members, with Omicron BA.5 as well as with BA.2 Spike proteins, prepared immune libraries again, and performed phage display using the Omicron BA.5 RBD as a bait. We obtained two new VHH antibodies of the Re32D03 class, namely Ma28H02 and

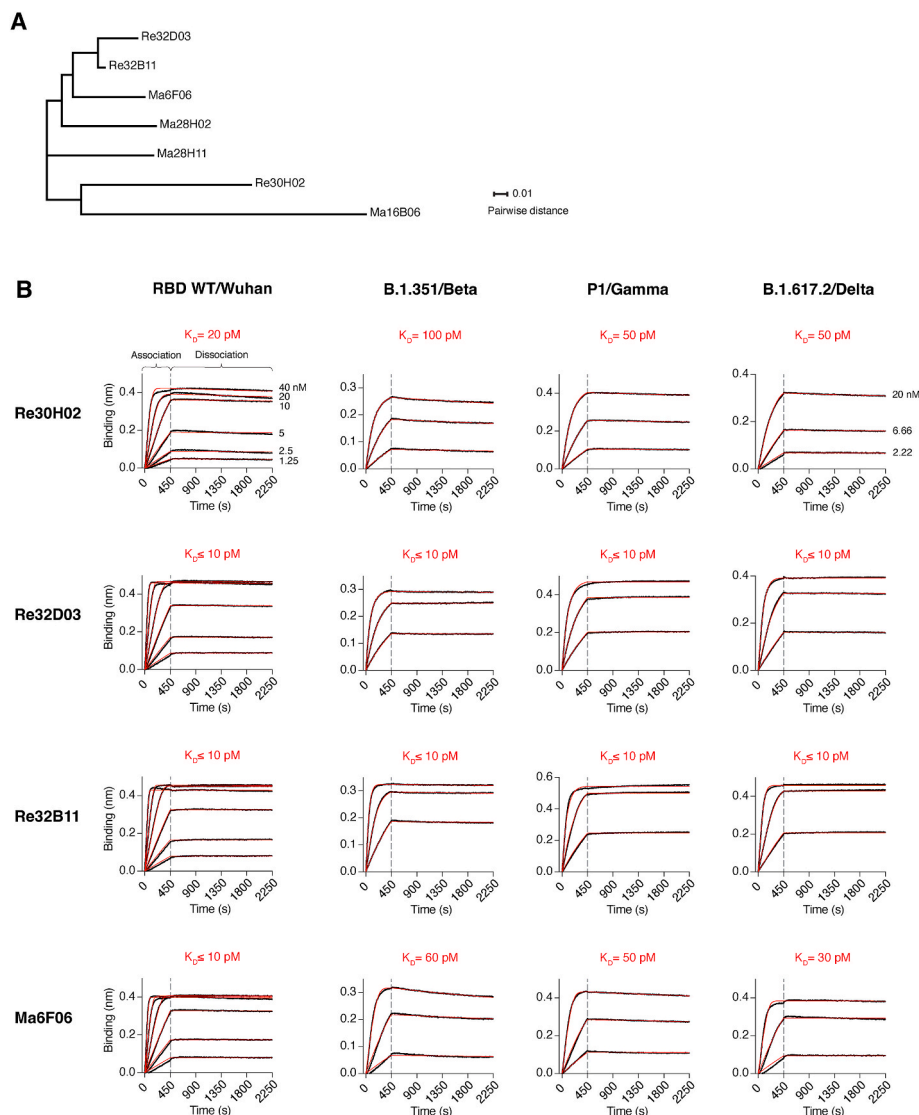


Fig. 1. Second generation nanobodies to the Spike proteins of SARS-CoV-2 variants **A.** Sequence relationship of second-generation anti-SARS-CoV-2 RBD nanobodies. The sequences of the nanobodies are provided in Suppl. Fig. 1. They were aligned using Clustal Omega (Sievers et al., 2011), and the phylogram was constructed with Dendroscope (Huson and Scornavacca, 2012). **B.** Affinities of nanobodies for the RBDs of SARS-CoV-2, Wuhan and variants Beta through Delta, determined by bio-layer interferometry (BLI). The indicated RBD constructs were immobilized on BLI sensors and dipped into solutions containing 2-fold (40, 20, 10, 5, 2.5, and 1.25 nM; for WT RBD) or 3-fold (20, 6.66, and 2.22 nM; for mutant RBDs) dilutions of nanobodies for 450 s. Then, nanobody dissociation in assay buffer was followed for 1800 s. The response curves (black) were fitted using a mass transport model to obtain K_D s. Fitted curves are shown in red.

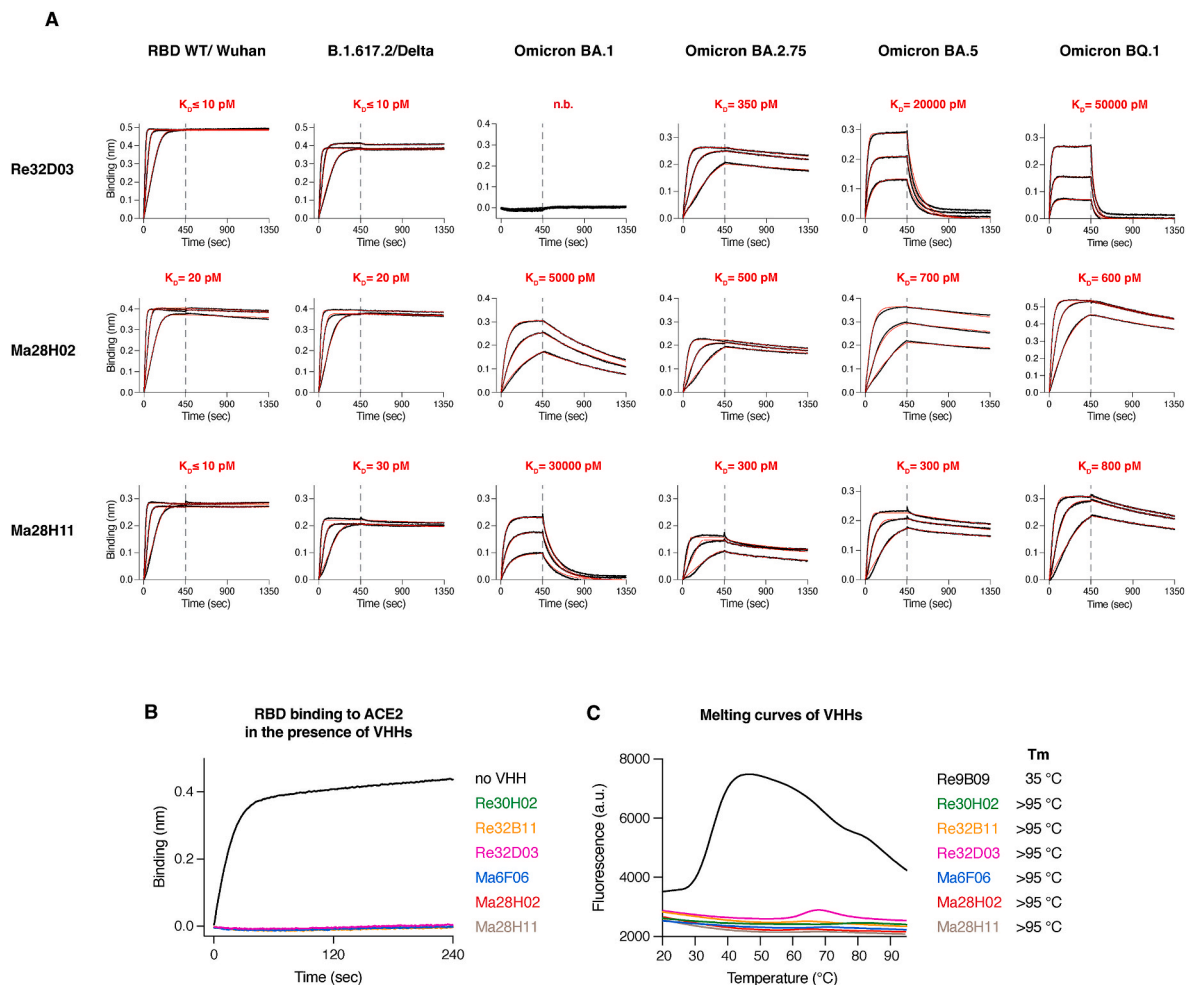


Fig. 2. Nanobodies binding to Omicron variants of SARS-CoV-2. Nanobodies described in Fig. 1A and Suppl. Fig. 1 were characterized as follows. **A.** Affinities towards the Spike protein-derived RBDs from the indicated Omicron variants, determined by BLI. RBD-loaded sensors were dipped into wells containing 100, 40, and 16 nM nanobody solutions for 450 s, and then incubated with assay buffer for 900 s. The response curves (black) were fitted using a mass transport model. Fitted curves are shown in red. **B.** Competition of nanobodies with ACE2 for binding the RBD. The Wuhan Spike RBD (50 nM) was incubated with nanobodies (500 nM), and binding to ACE2 (immobilized on the sensors) was monitored by BLI. **C.** Thermostabilities of nanobodies were analyzed by differential scanning fluorimetry (DSF) with a temperature range from 20 to 95 °C, in the presence of SYBR Orange. Unfolding is reflected by an increase in fluorescence, since the exposure of hydrophobic residues augments binding to the dye. Melting temperatures correspond to the inflection point of the melting curve before reaching the first melting peak. Stable proteins produce no melting peak. All nanobodies under study were stable at least up to 95 °C, whereas a previously described nanobody Re9B09 (Güttler et al., 2021) had a melting temperature of 35 °C.

Ma28H11 (Fig. 1A; Suppl. Fig. 1). Bio-layer interferometry (BLI) revealed high affinities towards the Omicron BA.5 RBD, with K_D values of 700 pM and 300 pM for Ma28H02 and Ma28H11, respectively (Fig. 2A). The two nanobodies also showed remarkable cross-reaction with RBDs of earlier VOCs, namely Wuhan/Wildtype, Delta, Omicron BA.1 as well as with Omicron BA.2.75 and BQ.1 RBDs. This surpasses the affinities of currently available conventional antibodies to the same Omicron variants (Moulana et al., 2023; Tuekprakhon et al., 2022; VanBlargan et al., 2022).

All newly selected nanobodies also blocked the RBD-ACE2 interaction (Fig. 2B). Moreover, all nanobodies showed remarkable hyperthermostability in differential scanning fluorimetry (DSF) analysis, resisting melting at 95 °C (Fig. 2C), which predicts a long shelf life and straightforward production (Goldberg et al., 2011; Jarasch et al., 2015). Thus, recent variants of SARS-CoV-2 are still amenable to nanobody binding, raising a promising perspective for future therapy of coronavirus infections.

2.2. Crystal structure analysis of nanobodies with the variant RBDs reveals extensive association interfaces

For a better understanding of how the newly developed nanobodies interact with the Spike, we elucidated the structures of two VHH class representatives, namely Re30H02 and the Re32D03 class member Ma6F06 (Fig. 1A), in complex with the Wuhan/Wildtype RBD. To this end, we employed a previously described nanobody-assisted folding strategy (Güttler et al., 2021) and produced RBD-fold promoter VHH complexes in *P. pastoris*, co-crystallized them with the nanobodies Re30H02 or Ma6F06, and solved their structures by X-ray crystallography (Fig. 3A–C). Both Re30H02 and Ma6F06 bind to the main epitope as defined by VHH Re5D06 of the RBD (see above) and clash frontally with ACE2 (Fig. 3A).

Interestingly, the nanobodies Re30H02 (Fig. 3B) and Ma6F06 (Fig. 3C) bound to the Wuhan RBD with similar orientations and interaction interfaces as Re5D06 (Fig. 3A; (Güttler et al., 2021)). When the structures are aligned with respect to the RBDs, the 106 C α atoms of the nanobody scaffolds essentially coincide, with root mean square deviations (RMSD) of 1.75 Å (Re5D06-Re30H02), 4.15 Å

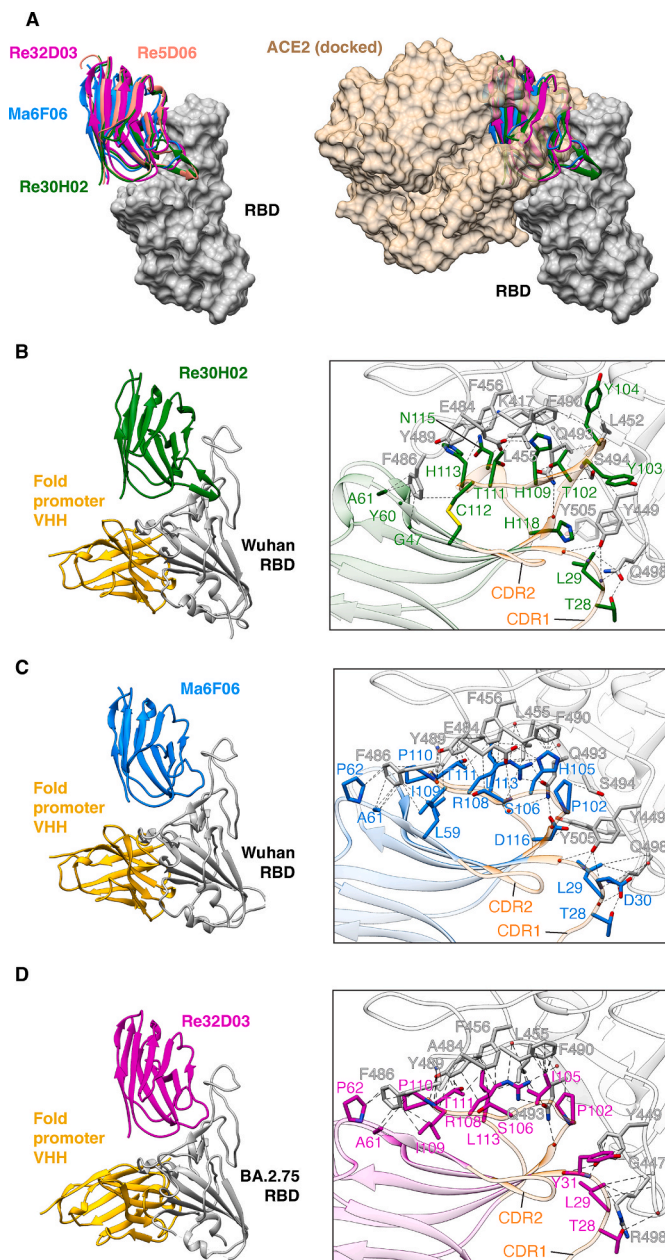


Fig. 3. Structural characterization of tertiary RBD•2xNanobody complexes. RBDs were co-expressed with a fold promoter VHH (Re5F10 or Ma3B12) which we had previously found to facilitate soluble RBD expression in *E. coli* and *P. pastoris* (Güttler et al., 2021) and co-crystallized with the indicated nanobodies. **A.** Crystal structures in **B, C, D** and the structure of Re5D06-RBD complex (PDB ID 7OLZ, Güttler et al., 2021) were overlaid with respect to the RBD. Fold promoter VHHs were omitted, and the RBD is represented as surface (Left). On the right, ACE2 (semi transparent brown surface) was docked onto the RBD, based on the alignment of the RBD with the SARS-CoV-2 RBD-ACE2 complex, PDB ID 7KMS (Zhou et al., 2020). Please note the extensive clashes of ACE2 with the nanobodies. **B-C-D.** Crystal structures of the Re30H02 (**B**), Ma6F06 (**C**), and Re32D03 (**D**) in complex with RBD•Fold promoter VHH are shown. Left: Overview of the tertiary complexes as ribbon representation. Right: Details of the nanobody•RBD interaction. The RBD and the nanobodies are shown as transparent ribbons, colored as on the left with CDR loops shown in orange. Interacting residues are shown as sticks, blue marks nitrogen, and red oxygen. Dashed lines link interacting atoms (distance ≤ 4 Å). Lines pointing onto backbones indicate contacts to amide or carbonyl groups.

(Re5D06-Ma6F06), and 3.6 Å (Re30H02-Ma6F06), respectively (Fig. 3A). The topologies and orientation of the long CDR3 loop is also very similar.

These nanobodies also contact almost identical residues of the RBD. These include three tyrosines (Y449, Y489, Y505), three phenylalanines (F456, F486, F490), and two glutamines (Q493 and Q498). The paratope on the nanobody side is formed by the CDR1 and CDR3 loops and several nanobody scaffold residues (Suppl. Fig. 1). It is striking that although there is no sequence similarity of CDR3s (Suppl. Fig. 1), the RBD interaction is still analogous for these three nanobodies.

Overall, the structures demonstrate tight interactions between the nanobodies and the RBD, which are consistent with their high affinities for the RBD (Fig. 1B). The structures also revealed how these nanobodies can tolerate escape mutations seen in Beta, Gamma, and Delta VOCs. For example, RBD residues K417, L452, and N501 are close to but not part of the Ma6F06 interaction interface, and their mutations/substitutions do not seem to induce steric clashes with the nanobody. RBD E484, on the other hand, forms a salt bridge with Ma6F06 H105, but the loss of this interaction may not be detrimental. This histidine residue is isoleucine in Re32B11 and Re32D03, and these bind Beta or Gamma RBDs better than Ma6F06.

The structures also revealed how nanobody binding might be affected by the Omicron mutations (Suppl. Figs. 2A and B). Among the 15 RBD mutations of BA.1, only 5, namely G446S, E484A, Q493R, G496S, and Q498R, are at the RBD-nanobody interface. Yet all nanobodies – Re30H02, Re32D03, Re32B11, Ma6F06 – completely failed binding to the BA.1 RBD in BLI experiments (for Re32D03, see Fig. 2A). Analysis of the RBD-nanobody structures indicate that the Q493R and Q498R RBD mutations could be critical, as these would create major steric clashes with the nanobodies. In fact, Q493R is reverted in several other Omicron VOCs, including BA.5, BQ.1, and BA.2.75 (though these have additional mutations), and Re32D03 binds their RBDs (Fig. 2). This suggests that the impact of Q493R might be more pronounced than that of Q498R. Newly selected Re32D03 class members Ma28H02 and Ma28H11 bind these RBDs, as well as the BA.1 RBD, much better than Re32D03 itself, indicating that subtle substitutions could improve the mutation tolerance of Re32D03.

To determine how Re32D03 can bind Omicron RBDs, and to understand how new class members can adapt to escape mutations seen in recent Omicron VOCs, we also determined the crystal structure of Re32D03 in complex with the BA.2.75 RBD (in the presence of a fold promoter nanobody; Fig. 3D). Re32D03 itself is almost identical to Ma6F06 (RMSD 0.6 Å over 127 C α atoms), and it recognizes analogous positions on the BA.2.75 RBD to that of Ma6F06 on the Wuhan RBD (Fig. 3C and D). Yet, when the structures are aligned with respect to the RBDs, the difference in nanobody positioning becomes apparent (RMSD 4.5 Å over all C α atoms; Fig. 3A). The Re32D03 CDR1 loop is tilted away approximately 6°, probably to accommodate the RBD Q498R substitution, where arginine now interacts with Re32D03 T28 (Fig. 3D). This might suggest that the nanobodies could accommodate Spike variations without obvious changes in their sequence.

BA.5 and BQ.1 Spike has two noteworthy mutations compared to BA.2.75, namely L452R and F486V. The former is also seen in the Delta variant and well tolerated by Re32D03. It is close to but not at the interaction interface. F486, on the other hand, extensively interacts with Re32D03 (Fig. 3D), and F486V could dramatically reduce the binding energy. Likewise, BLI experiments with the BA.5 and BQ.1 RBDs show very fast dissociation of Re32D03. A tight binding is, however, restored in the Re32D03 class members Ma28H02 and Ma28H11 (Fig. 2A). Yet, comparison of the sequences does not provide a direct clue. They do not have any substitutions that could directly compensate F486V. In fact, most of the substitutions in Ma28H02 and Ma28H11 are in the nanobody framework or in the CDR2 loop (Suppl. Fig. 1) and thus not part of the paratope. However, two positions are particularly interesting, CDR3 prolines 102 and 112. The two common changes seen in Ma28H02 (P102S and P112T) and Ma28H11 (P102V and P112V) do not contribute

directly to binding, but we envision that the substitutions of the prolines could provide additional flexibility at CDR3 to adapt to changes at the RBD.

Importantly, the interfaces between so far characterized nanobodies and the Spike proteins always clashed with the interaction surfaces of the ACE2 receptor and the Spike (Fig. 3A), explaining how nanobodies and ACE2 compete for binding to the Spike, and anticipating strong neutralization by the nanobodies.

2.3. Nanobodies efficiently neutralize SARS-CoV-2 variants at picomolar concentrations

To determine the neutralization potencies, we preincubated serial dilutions of Re30H02, Re32B11, Ma6F06, or Re32D03 with cell supernatants containing a Wuhan-like strain (Stegmann et al., 2021) or the Alpha or Delta variants of the virus. The mixtures were then added to a fresh monolayer of Vero E6 cells. 48 h later, infection was monitored by RT-qPCR, to quantify replicated viral RNA (Fig. 4A), or by direct counting of infected cells by immunofluorescence detection of newly

synthesized spike components (Fig. 4B; Güttler et al., 2021). All nanobodies conferred complete neutralization of all three strains, with IC99 inhibitory concentrations being in the 100 pM range (Fig. 4C) – although there was some strain-specific variation. Re32D03, for example, was the most potent Delta neutralizer.

In a different setup, we infected Vero E6 cells the Wuhan strain in the presence of Re32D03, and observed that 0.17 nM nanobody was sufficient for a complete suppression of infectious particle release (Fig. 4D; Suppl. Table 2). These results support the notion that the nanobodies not only bind to the Spike-RBDs of SARS-CoV-2 Alpha and Delta but also neutralize their ability to infect cells.

Using similar assays as above, we found that the nanobodies Ma28H02 and Ma28H11 are highly potent neutralizers of the Wuhan and Delta strains. The two also neutralized the BA.5 Omicron variant (Fig. 5A–C). However, a 5 nM concentration was required for a clear effect. Given the low affinity of most Omicron variants for currently available antibodies (Moulana et al., 2023; Tuekprakhon et al., 2022; VanBlargan et al., 2022), these results still raise hopes for the use of anti-Omicron nanobodies in the clinics.

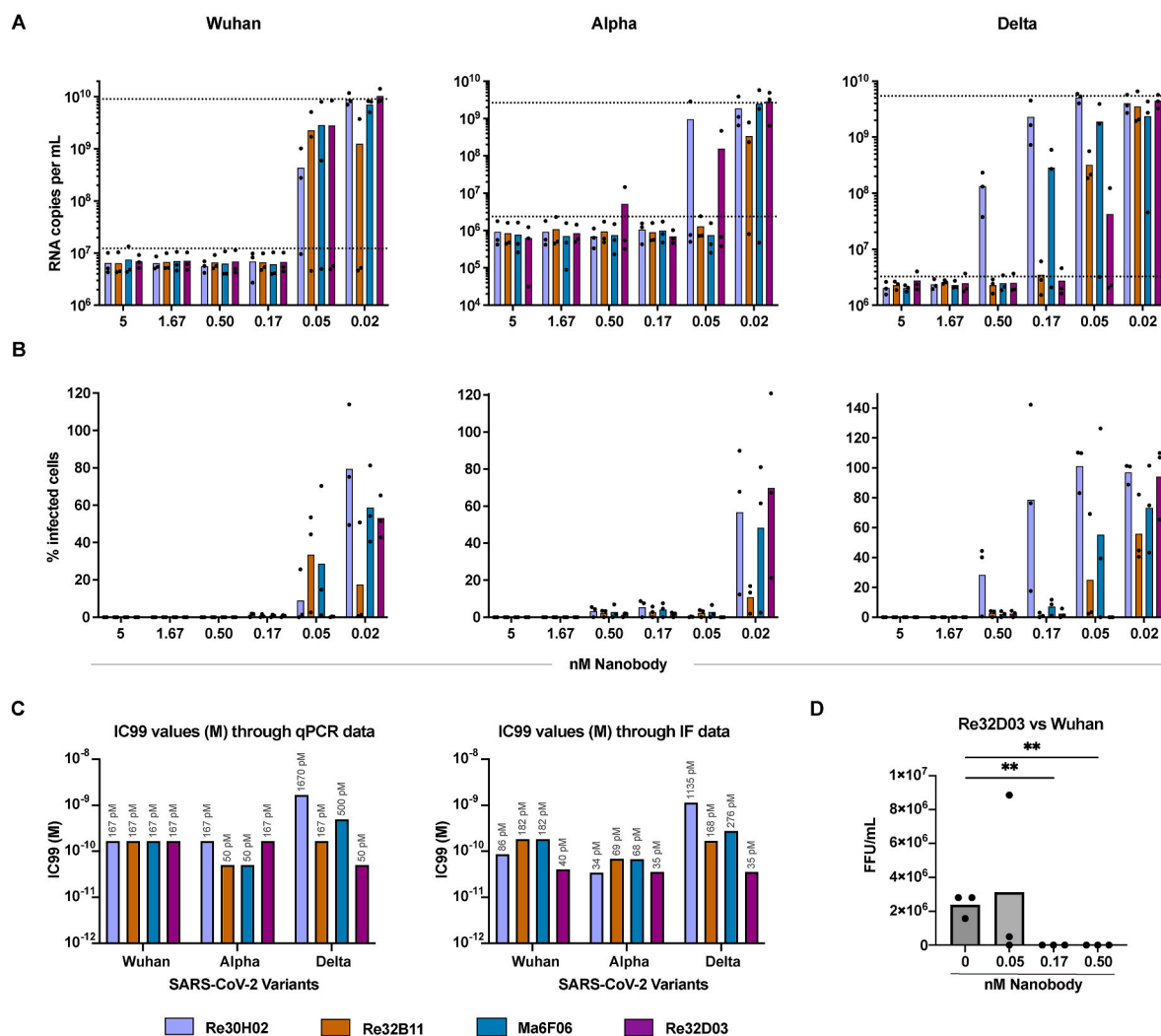


Fig. 4. Neutralization of SARS-CoV-2 variants Alpha and Delta by nanobodies. A Wuhan-like strain of SARS-CoV-2 or its Alpha or Delta variants were incubated with indicated concentrations of Re30H02, Re32B11, Ma6F06 and Re32D03, and then used to infect Vero E6 cells. A. Forty-eight hours later, the amount of virus-derived RNA in the culture supernatant was determined by RT-PCR. Viral RNA present in the inoculum and detected after 48 h were marked with lower and upper dotted lines, respectively. B. Cells were stained with sets of anti-RBD and anti-S1ΔRBD nanobodies (Güttler et al., 2021), the fraction of infected cells was then quantified by confocal laser scanning microscopy. C. Nanobody concentrations that diminished virus RNA or infected cells by 99% (IC99) are displayed. D. SARS-CoV-2 (Wuhan)-containing cell culture supernatants, collected after infecting Vero E6 cells with the virus in the presence of different concentrations of nanobody Re32D03 for 48 h, were serially diluted in media and used to infect fresh VeroE6 cell monolayers. Infected cells were identified as in (B) and fluorescence forming units (FFU) per mL of each virus-supernatant were determined using the TCID50 calculator (Marco Binder, University of Heidelberg).

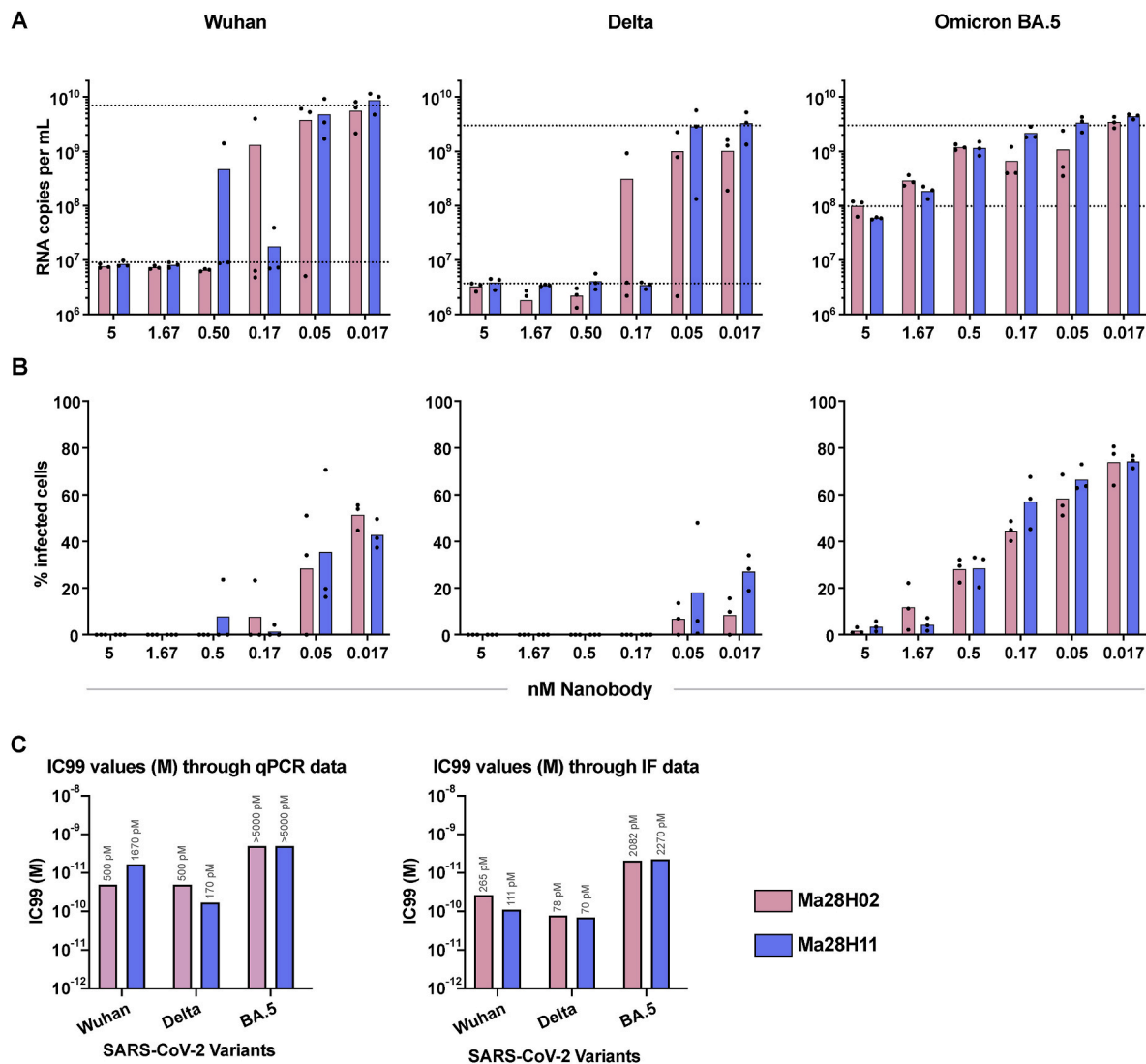


Fig. 5. Neutralization of SARS-CoV-2 Omicron variants by nanobodies. A–C Neutralization of SARS-CoV-2, Delta and Omicron BA.5 variants by Ma28H02 and Ma28H11. The neutralization experiment and the analyses were performed as described in Fig. 4A–C.

To assay neutralization of more recent SARS-CoV-2 variants, we pseudotyped a Vesicular Stomatitis Virus (VSV) with Spikes of the Omicron BA.2, BA.2.75, BA.4/5, BQ.1, BJ.1, and XBB.1 variants. The recombinant VSV genome encodes here a green fluorescent protein (GFP) to visualize cells that become infected upon incubation with the pseudotype (Zimmer et al., 2014).

Preincubation with the Re32D03 class member Ma28H11 blocked infection by the BA.2.75 pseudotype already at a sub-nanomolar concentration (Fig. 6A and B). Indeed, Ma28H11 was the most potent neutralizer of this variant (Fig. 6C and D). Re32D03 also neutralized BA.2.75 quite well, consistent with our crystal structure (Fig. 3D). Likewise, Ma28H11 was quite effective ($IC_{99} = 5$ nM) against BA.4/5. However, it showed little effect against the BJ.1 and XBB.1. These two variants share the F490 mutation (F490V in BJ.1 and F490S in XBB.1), which eliminates a central nanobody-RBD contact not only in the Re32D03 class (shown for Ma6F06 and Re32D03 in Fig. 3C and D) but also in Re30H02 (Fig. 3B), Re5D06 (Güttler et al., 2021; Zibat et al., 2023) and indeed in numerous nanobodies that target this epitope (Ahmad et al., 2021; Koenig et al., 2021a). This thus represents a very challenging escape mutation.

2.4. A nanobody neutralizes through simultaneous interaction with two RBDs of a spike trimer

By phage display, we also selected the nanobody Ma16B06, which represents a class that is unrelated to those described above (Fig. 1, Suppl. Fig. 1.). It binds the RBD of the Wuhan and the BA.1, BJ.1 with low pM affinities, and XBB.1 with still 250 pM affinity (Fig. 7A). It thus appears to tolerate the F490 mutation. It also neutralized Omicron BA.1 already at a concentration as low as 50 pM (Fig. 7B and C).

To understand this mode of RBD recognition, we crystallized the BA.1 RBD in complex with a fold promoter nanobody and Ma16B06. The solved structure revealed that Ma16B06 binds the RBD in a different topology and with a shifted epitope as compared to Re32D03 (Fig. 7E). The steric clash with ACE2 is much smaller, but still sufficient for neutralization.

The interface on the nanobody side includes all three CDRs as well as several scaffold residues. On the RBD side, it avoids most of the residues that have been subject to immune escape mutations in early virus variants (e.g., the original K417, T478, E484, and N501 residues are not contacted). In fact, among the 15 mutated residues seen in Omicron BA.1 (Suppl. Fig. 2), Ma16B06 interacts with only two, G446S and Q498R (Fig. 7F), where the arginine now engages in a perfect cation- π interaction with F58 of the nanobody's CDR2.

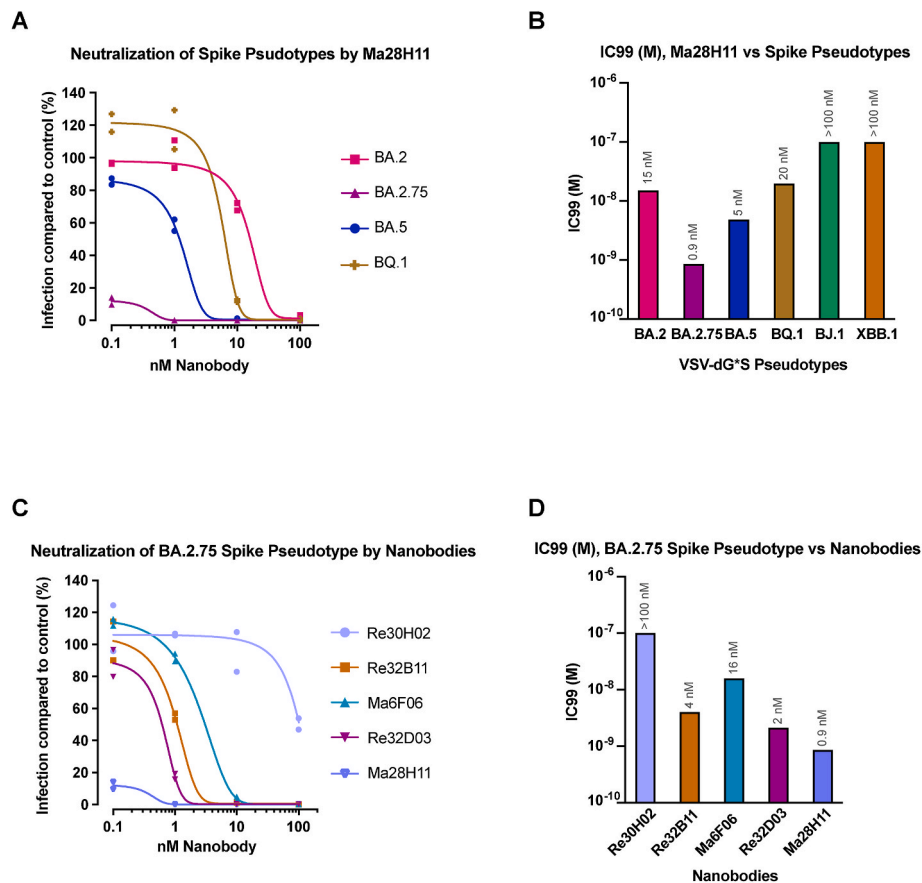


Fig. 6. Neutralization of pseudotyped SARS-CoV-2 by nanobodies. A recombinant version of Vesicular stomatitis virus (VSV), capable of encoding green fluorescent protein (GFP), was pseudotyped to carry the Spike proteins of the indicated SARS-CoV-2 variants on its surface, as described previously (Zimmer et al., 2014). The virus, pre-incubated with indicated concentrations of nanobodies, was used for inoculation of Vero E6 cells, and the percentage of GFP-expressing (and thus infected) cells was determined. A. Neutralization of the indicated SARS-CoV-2 Omicron Variants by the nanobody Ma28H11. B. Calculated IC99 values in (A) including BJ.1 and XBB.1 neutralization are shown. C. Neutralization of the SARS-CoV-2 Omicron BA.2.75 variant by indicated nanobodies. D. IC99 values of (C) are plotted.

However, F490, Y449, and L452 of the RBD are directly recognized, though the F490 contact is not as central as for the nanobodies described above. This is consistent with the observation that the XBB.1 RBD (carrying an F490S exchange) binds Ma16B06 with a reduced affinity of 250 pM (Fig. 7A). Likewise, a higher nanobody concentration of 10 nM is required for complete neutralization (Fig. 7D).

The Delta variant harbors an L452R mutation, which causes major steric clashes that would force the arginine to a restrained rotamer. This results in a complete loss of binding (Fig. 7A). BA.5 carries the same mutation but still shows clear binding with a low nM KD, suggesting that other exchanges favor the interaction. The aforementioned cation- π interaction of Q498R with F58 of the nanobody falls into this category. The omicron variants BA.2.75 and BJ.1 are well recognized and neutralized, indicating that their additional mutations are not detrimental to nanobody binding (Fig. 7A, D).

We were also interested in analyzing the interaction of Ma16B06 with a complete BA.1 Spike trimer and therefore solved a cryo-EM structure of the corresponding complex (Fig. 7G). The EM reconstruction revealed a 1-up and 2-down RBD conformation, which is characteristic of the Omicron spike (Cui et al., 2022). All three RBDs are occupied by Ma16B06.

It is known that only the RBD in up conformation can bind ACE2 and thus promote virus entry. This single up-RBD is blocked in two ways: by the nanobody bound directly to it and by the nanobody bound to a neighboring down RBD. In fact, the latter nanobody causes the more extensive steric clash with ACE2 (Fig. 7G). It may also bind with higher affinity because it makes additional contacts to neighboring protomers. These include potential h-bonds and a salt bridge (to the neighboring

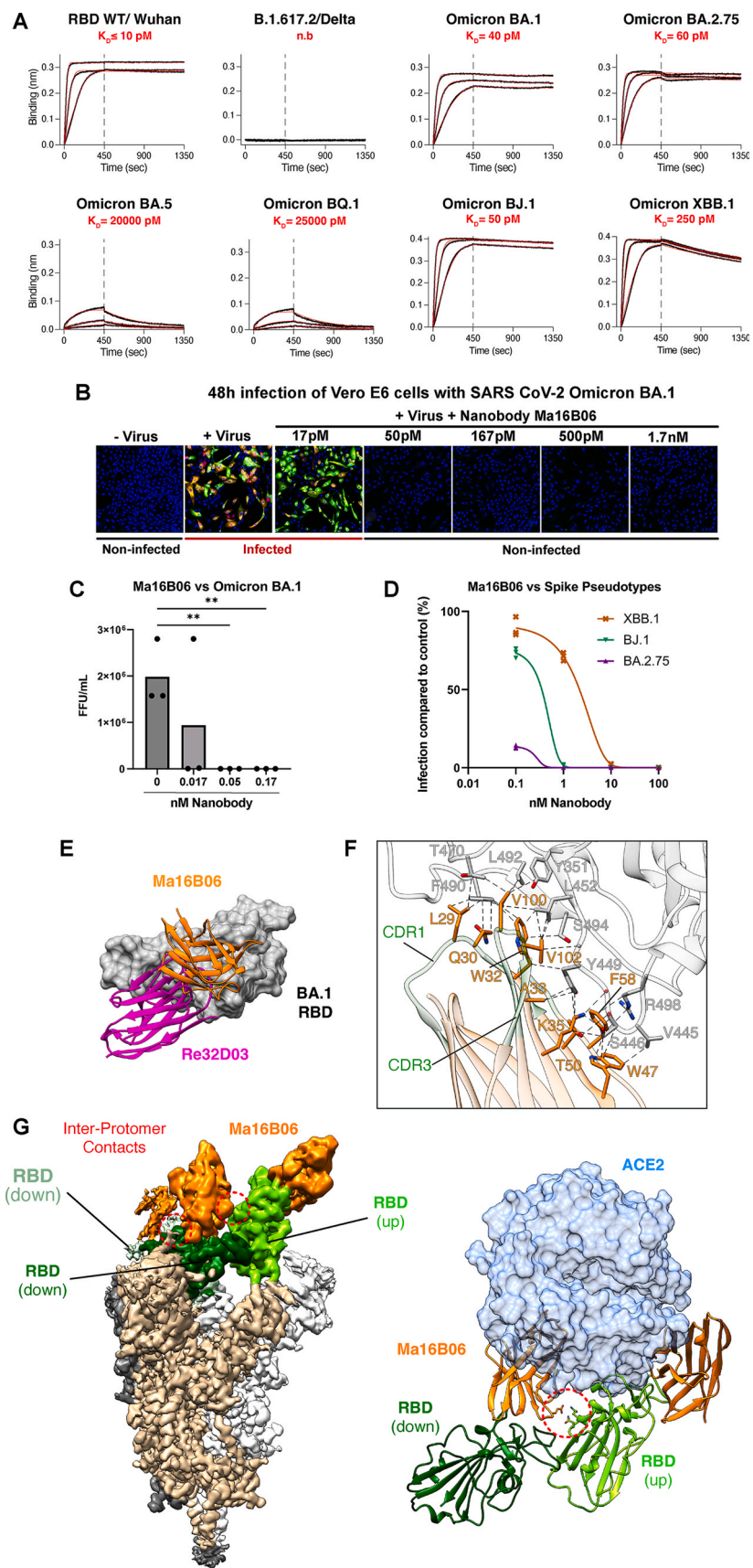
RBD) as well as weak contacts to a glycan of a neighboring NTD domain. Thus, a single molecule of Ma16B06 may be sufficient to neutralize the trimeric Spike protein.

2.5. Aerosolized nanobody retains neutralizing capacity

Having obtained neutralizing nanobodies against SARS-CoV-2 Spike proteins, we next sought to identify a suitable application route for prophylaxis and therapy of COVID-19. Respiratory epithelia represent the primary infection site, and we thus established a delivery system to cover these epithelia with nanobody.

The first step towards this goal consisted in an optimized and reproducible production scheme, suitable for upscaling (Suppl. Fig. 3). For producing Re32D03, we used an expression system based on *Pichia pastoris*, now more correctly termed *Komagataella phaffii*. This organism is not only known for high yields of recombinant protein synthesis, but also for its ability to grow on methanol as a carbon source. We integrated a methanol-inducible Re32D03 expression cassette into the Aox1 locus. Upon induction, the nanobody was secreted from these cells into the culture supernatant to final concentrations of 3 g/L, suitable for further purification (Suppl. Fig. 4, Suppl. Fig. 5). Pharmacokinetic analyses after intratracheal application in rats revealed that detectable amounts of nanobody remained in the lung for at least 24 h (Suppl. Table 1).

For moving closer to clinical applications through inhalation, we employed a newly adapted (Pohlmann et al., 2018) vaporizing system for aerosol formation. Nanobody solutions containing Re32D03 were fed into a dispersion nozzle and dispersed by pressurized air into a mixing chamber, from where aerosols were released to animal cages for



(caption on next page)

Fig. 7. Neutralization of SARS-CoV-2 with a nanobody that binds two RBDs within a Spike simultaneously **A.** Ma16B06 affinities were determined by BLI as described in Fig. 2A using the indicated RBD-loaded sensors. **B.** Vero E6 cells were infected with SARS-CoV-2 Omicron BA.1, pre-incubated with indicated concentrations of Ma16B06. Cells were fixed two days after inoculation, stained with sets of anti-RBD (green) and anti-S1ΔRBD (red) nanobodies and analyzed by CLSM. **C.** The TCID₅₀ was measured as in Fig. 4D, determining the infectious units obtained when infecting Vero E6 cells with SARS-CoV-2 Omicron BA.1 in the presence of nanobody Ma16B06 at the indicated concentrations. **D.** A recombinant version of Vesicular stomatitis virus (VSV), capable of encoding green fluorescent protein (GFP), was pseudotyped to carry the Spike proteins of the indicated SARS-CoV-2 variants on its surface, as described previously (Zimmer et al., 2014). Upon incubation with Ma16B06 at various concentrations, the virus was used for inoculation of Vero E6 cells, and the percentage of GFP-expressing (and thus infected) cells was determined. **E.** Comparison of the Ma16B06 and Re32D03 epitopes on RBD. Crystal structure of the Ma16B06 in complex with Omicron BA.1 RBD was overlaid with the Re32D03•RBD complex aligning via the RBDs. Fold promoter VHs are omitted for clarity. Nanobodies are shown as ribbon and RBD as surface representations. **F.** Details of the Ma16B06•Omicron BA.1 RBD interaction. The RBD and the nanobody are shown as transparent ribbons, colored as in (E) with CDR loops shown in green. Interacting residues are shown as sticks, blue marks nitrogen, and red oxygen. Dashed lines link interacting atoms (distance ≤ 4 Å). Lines pointing onto backbones indicate contacts to amide or carbonyl groups. **G.** Cryo-EM reconstruction of the SARS-CoV-2 BA.1 Spike•Ma16B06 complex. Left: SARS-CoV-2 BA.1 Spike was mixed with an excess of Ma16B06, purified by size exclusion chromatography, and vitrified immediately for structure determination by cryo-EM. The shown map is a composite of two volumes that were refined to high resolution through MultiBody refinement in Relion (Suppl. Fig. 11). The Spike protomers are displayed in gray, tan, or white, respectively, and are further color-coded as indicated. The densities for Ma16B06 are highlighted in orange. Regions of inter-protomer contacts that involve Ma16B06 are circled in red (see text for details). Right: The crystal structure of the RBD•Ma16B06 complex (shown in ribbon representation) was modeled into the RBD•Ma16B06 densities (overall resolution of 3.6 Å; Suppl. Fig. 12), and colored as indicated. Residues at the inter-protomer Ma16B06•RBD interface (Ma16B06 E56; RBD R408; Q414) are shown as sticks and circled in red. ACE2 (shown as a semi-transparent blue surface) was docked to the RBD in the “up” conformation, based on the alignment of the RBD with the SARS-CoV-2 RBD•ACE2 complex, PDB ID 7KMS (Zhou et al., 2020). See text for details.

inhalation (Fig. 8A; Suppl. Fig. 6A). Droplet sizes were reproducibly distributed to reach all compartments of airways, including the lower bronchi and alveoli (Suppl. Fig. 6B; Suppl. Table 3).

Most proteins become denatured when exposed to air-liquid interfaces, and aerosols display a particularly high ratio of surface to volume. On the other hand, the thermostability of the nanobody at least suggests that it might also withstand the challenge of surface exposure. To assess whether the nanobody retains its neutralization capacities within aerosols, we recovered the droplets from the aerosol and tested this preparation for virus neutralization. As shown in Suppl. Fig. 6C, the nanobody had retained most of its neutralization capacity. This indicates that it is still active within the aerosol and tolerant to shearing forces within the nebulizer.

2.6. Prophylactic and therapeutic exposure to aerosols containing nanobodies confers near-complete protection of hamsters against SARS-CoV-2 infection and COVID-19

To test the capability of the nanobody to prevent infection, we exposed hamsters repeatedly with nanobody-containing aerosols (Fig. 8B; Suppl. Figs. 7A and B; Fig. 8A and B; Suppl. Table 4). In the prophylactic group, 3 h after the first administration of nanobodies, the animals were challenged with an intranasal application of SARS-CoV-2. In the absence of nanobodies, the animals soon displayed the typical signs of COVID-19 and lost weight. In contrast, the nanobody-exposed animals were almost completely protected and displayed significantly lower weight loss (Fig. 8C). This strongly argues that the nanobody inhalation was highly efficient for prophylaxis against SARS-CoV-2 infection. Moreover, we asked whether the nanobodies might still reduce the severity of COVID-19, even when administered after onset of the infection. To test this, we first infected animals and allowed the virus to spread within their airways for 24 h. Afterwards, the animals were exposed to aerosols containing the nanobody Re32D03, at three different concentrations. Compared to previous literature (Nambulli et al., 2021), this is by far the latest time that nanobody-based inhalation therapy was attempted in a preclinical model. Strikingly, despite the late treatment, the nanobodies led to a marked recovery, at all concentrations tested (Fig. 8C). Treated animals had a much milder loss in weight.

On day 6 post infection, the animals were euthanized to determine the extent of infection and COVID-related parameters. PBS-treated and infected hamsters as well as all therapeutically treated and infected dose groups displayed alterations associated with COVID in varying degrees of severity (Fig. 9A and B, and Suppl. Figs. 8 and 9). Alveolar lesions were characterized by multifocal areas of infiltration of mainly neutrophils and macrophages, necrosis of alveolar epithelium, fibrin extravasation, alveolar edema and hemorrhage as well as multifocal

regeneration of alveolar pneumocytes with presence of large and/or multinucleated cells. Within the conductive airways, multifocal bronchitis/-iolitis and peribronchial/-iolar cuffing with areas of epithelial regeneration were detected. Nanobody inhalation was able to reduce these pathologies, especially when used in a prophylactic fashion where significantly less inflammatory and regenerative changes were present (Fig. 9A and B, and Suppl. Figs. 8 and 9). However, vascular lesions characterized by endothelialitis, vasculitis, perivascular cuffing, edema and hemorrhage remained prominent in all groups with a significant decrease in the prophylactically-treated hamsters (Suppl. Fig. 8).

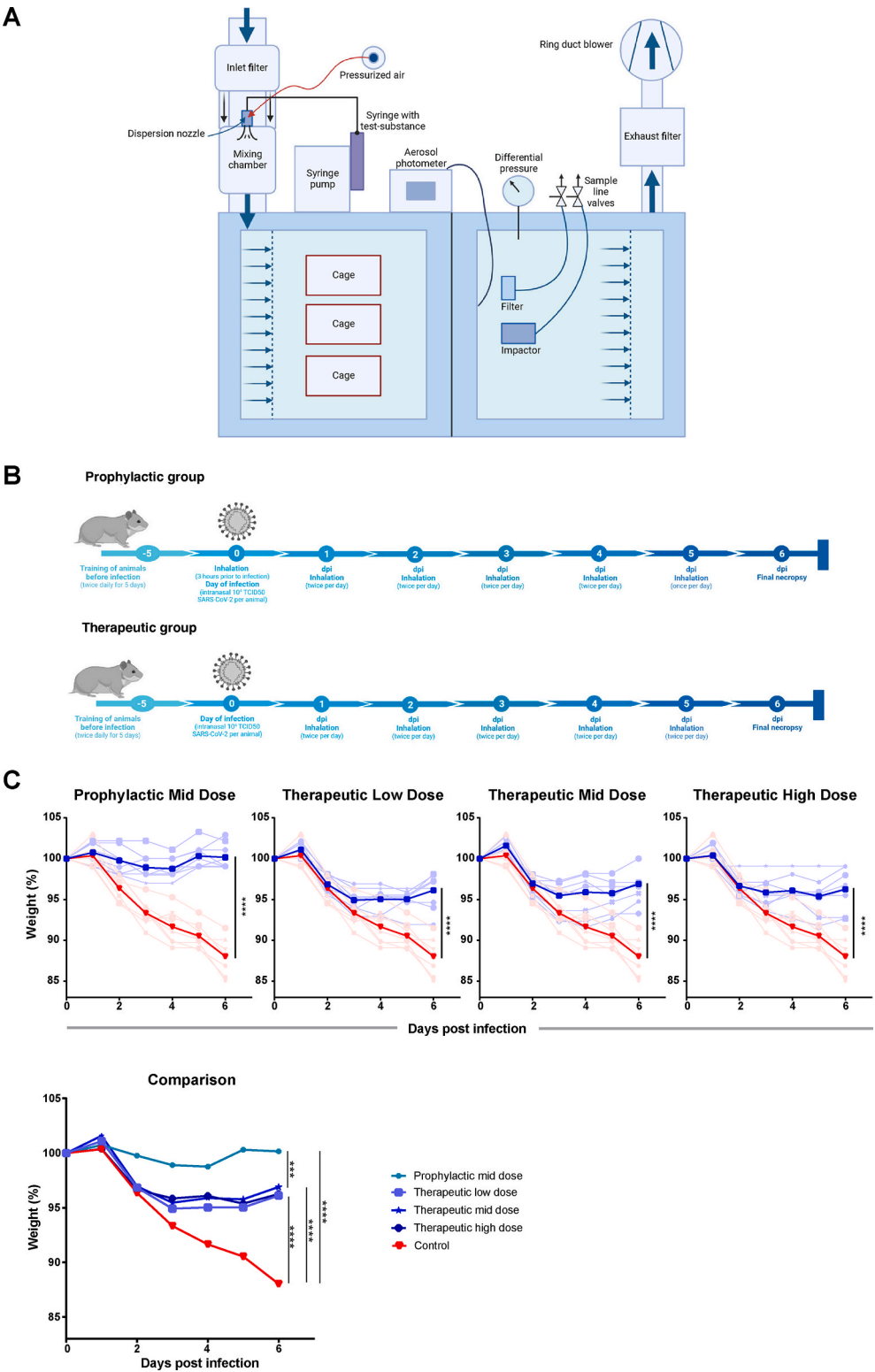
To further corroborate the protective effect of nanobodies, we next analyzed the blood of the animals at day 6 post infection. Blood chemistry revealed a trend towards diminished alterations upon antibody inhalation, albeit with large variations between animals (Suppl. Fig. 10A, Suppl. Table 5). Strikingly, however, granulocyte levels were raising in response to the infection in otherwise untreated control animals, but only to a significantly lesser extent in nanobody-treated animals (Suppl. Fig. 10B). Thus, the inflammatory response associated with COVID-19 was diminished by nanobodies when administered prophylactically or therapeutically. This does not imply that the nanobody would directly interfere with the inflammatory response. Rather, we propose that the nanobody was reducing the spread of the virus, and that reduced inflammation was a secondary consequence of diminished amounts of virus.

When measuring the amount of SARS-CoV-2 RNA in bronchial lavage fluid (BALF), this was detectable but strongly reduced upon prophylactic or therapeutic use of nanobodies, compared to infected but untreated animals (Fig. 9C). Perhaps most strikingly, when we determined virus titers in the lungs of the animals, we found that only the infected but untreated animals still had detectable virus in their lungs. Thus, when assessing the TCID₅₀ in the lung necropsies, all nanobody-treated animals, regardless of administration time and dose, were free of infectious virus (Fig. 9D). These results further support the notion that the inhalation of nanobodies, before or after infection, provides extensive protection against the infection with SARS-CoV-2.

In summary, the inhalation of a nanobody directed against the SARS-CoV-2 Spike protein largely protects against infection in a prophylactic and even in a therapeutic setting, and it almost completely eliminates infectious virus. This raises the expectation that nanobody inhalation before or shortly after accidental exposure represents a viable strategy to avoid COVID-19 in humans.

3. Discussion

Our results demonstrate that inhaled nanobodies can effectively



(caption on next page)

Fig. 8. Aerosols containing the nanobody Re32D03 provide protection against SARS-CoV-2 infection in a hamster model **A.** Graphical representation of a device for aerosol formation. A photographic depiction of the device is provided in [Suppl. Fig. 6A](#). Nanobody solutions were fed into a nozzle and dispersed by pressurized air into the mixing chamber. Aerosols were then released to hamster cages. Aerosol concentration was monitored continuously by photometry. Continuous flow and controlled pressure were ensured by an exhaust system. **B.** Timeline of infections and aerosol treatments. Hamsters were infected intranasally with SARS-CoV-2 (Wuhan) and exposed to Nanobody Re32D03-containing aerosols at the indicated time points. For a therapeutic setting, the first nanobody inhalation was carried out 24 h after infection and then on consecutive days until euthanasia at day 6 post infection. Nanobody was used in different concentrations: vehicle without nanobody; low, medium and high concentration (for quantities, cf. [Suppl. Table 3](#)). For a prophylactic setting, the hamsters were first exposed to nanobody in aerosols at medium concentration, then infected, and then treated with aerosols as above. **C.** Weight loss of SARS-CoV-2-infected animals, indicating the severity of COVID-like disease. Each treatment group is shown in comparison to the control group treated with vehicle only. The weight of each animal is shown in a semi-transparent fashion, whereas the medium weight of the animals is shown in full color. The last panel summarizes the medium weight of all groups together. Weight loss of vehicle-treated animals was diminished by all therapeutic regimens, and it was entirely avoided by prophylactic exposure to nanobody-containing aerosols.

neutralize SARS-CoV-2 and display prophylactic and therapeutic efficacy in a preclinical model. The perspective of this is the use of nanobody by self-inhalation in humans, to prevent or to treat COVID-19 and other respiratory infections. We propose that nanobody-based therapy will be useful for non-hospitalized patients, to prevent deterioration of the disease, and as a prophylactic regimen for healthy individuals at risk of exposure to the virus.

The emergence of SARS-CoV-2 variants that escape neutralization by nanobodies or other antibodies represents an ongoing challenge. For successful antibody therapy, this requires the development of novel nanobodies that bind despite the corresponding mutations of the RBD. The nanobodies described here are capable of neutralizing a broad spectrum of virus variants. Moreover, selecting nanobodies from existing phage libraries allows the rapid identification of neutralizers to variants that might occur in the future. This provides a tool for tackling the emergence of novel variants of concern, ideally within a few weeks.

The panel of virus-neutralizing nanobodies shown in here, when taken together, not only corroborates the option of covering a wide spectrum of SARS-CoV-2 variants. It also exemplifies the “return” of virus variants to nanobody sensitivities that they had lost before. For instance, nanobody Ma28H11 neutralizes the Wuhan and Delta strains, fails in Omicron BA1 neutralization, but does neutralize BA2.75 and (to some extent) BA.5 ([Figs. 5 and 6](#)), which emerged later in the pandemic. It is tempting to speculate that the limited “sequence space” for RBD variation and the constraint on the virus to maintain an interaction with the cellular receptor ACE2 will limit escape mutations to a finite and manageable number. We propose that an arsenal of nanobodies, raised against variants of coronaviruses as well as other microbes causing respiratory infections, is suitable to increase pandemic preparedness. Such a collection of nanobodies could provide off-the-shelf options to combat newly arising diseases. Moreover, the corresponding phage libraries, if stored in collections, would allow the immediate selection of neutralizing agents against emerging virus variants.

Well-neutralizing, high-affinity anti-RBD nanobodies of the first generation, such as Re5D06 (isolated 6 weeks after the first immunization) had remarkably tyrosine-rich paratopes. This is consistent with the notion that tyrosines appeared as particularly interaction-prone residues, e.g., during selections from synthetic antibody libraries ([Koide and Sidhu, 2009](#)). Paratope-tyrosines thus allow for an effective initial immune response. The downside is, however, that tyrosines are likewise prone to promiscuous interactions ([Frey et al., 2018](#)). In antibodies, this could lead to off-target interactions and/or susceptibility to unspecific competition (for example by serum proteins).

After several rounds of additional immunization, the Re32D03 class became the dominant neutralizing class. Here, it is remarkable that the potentially promiscuous tyrosines in the paratope were largely replaced by less sticky residues ([Suppl. Fig. 1](#)) that now confer more sophisticated hydrophobic contacts (for example: Re32D03 T111 and I105; [Fig. 3D](#)) We suspect that the features selected during affinity maturation here were a higher effective affinity as a result of less non-specific competition, and perhaps also a better folding behavior. Indeed, while only a subset of the initially selected nanobodies were resistant to extreme heat

(>95 °C), hyperthermostable nanobodies became prevalent in later selections.

Inhaled antibodies offer several advantages over injected antibodies against respiratory viruses. Most importantly, inhaled antibodies are capable of capturing their targets right at the primary site of infection, the respiratory epithelia. This can potentially prevent initial infection, as seen in our study where prophylactic nanobody inhalation led to near-complete protection in animals. Prophylactic use of antibodies or nanobodies against SARS-CoV-2 by inhalation has been reported previously ([Esparza et al., 2022](#); [Gai et al., 2021](#); [Nambulli et al., 2021](#); [Piepenbrink et al., 2021](#)), and some of these studies also revealed ‘therapeutic’ efficacy when applying the antibody as early as 6 h after infection ([Nambulli et al., 2021](#); [Piepenbrink et al., 2021](#)). The uniqueness of our study consists in a) the set of high-affinity nanobodies with broad activity against multiple variants of SARS-CoV-2 and b) the therapeutic efficacy even when applying aerosols only 24 h post infection. Even when infection has already taken place, inhaled nanobodies can still be effective, as the virus spreads along respiratory epithelia, shedding from infected cells into the lumen and infecting other cells ([Kiener et al., 2021](#)). Such intraluminal virus spread is amenable to the neutralization by inhaled antagonists. We propose that this explains the remarkable finding of inhaled nanobodies antagonizing the infection even when applied as late as 24 h post infection.

Translating this treatment concept to humans will require the development of aerosols outside of the lab. A number of devices have been developed to achieve this ([Ari and Fink, 2020](#); [Dolovich and Dhand, 2011](#); [Longest et al., 2019](#)). Typically, a few puffs of aerosols are generated by pressing a small device, and those are inhaled immediately. Unlike animals, humans can deliberately inhale an aerosol and hold their breath for a few seconds subsequently, and this will make the application of nanobody-containing aerosols far more efficient than the exposure of whole animals to nebulized nanobody throughout their cages. Still, care must be taken to achieve optimal droplet sizes. Ideally, a spectrum of droplets should be generated, to cover both upper airways, i.e., large bronchi, as well as lower airways and even alveoli. Even when nanobodies reach these sites in the lungs, they may be eliminated through resorption, retrograde transport, or enzymatic degradation. However, our study found that nanobodies remained in the lungs of experimental animals for several hours, indicating their biological stability in the lungs.

Our approach has the potential of serving as a prophylactic strategy against SARS-CoV-2 infection, but only within certain limitations. It would be useful in a defined pre- or post-exposure setting, but not over an extended period such as the entire winter. For more long-term prophylaxis, active vaccinations are still required. Moreover, an affordable device to achieve suitable droplet size needs to be in place, avoiding over-dosage during self-application. Finally, it should be noted that established, severe Covid-19, will not be amenable to our treatment strategy, since hyperinflammation is the key pathomechanism at this stage. In summary, the perspective of therapeutically using anti-Spike nanobodies consists in a setting where the onset of the infection, not its progression, can still be avoided.

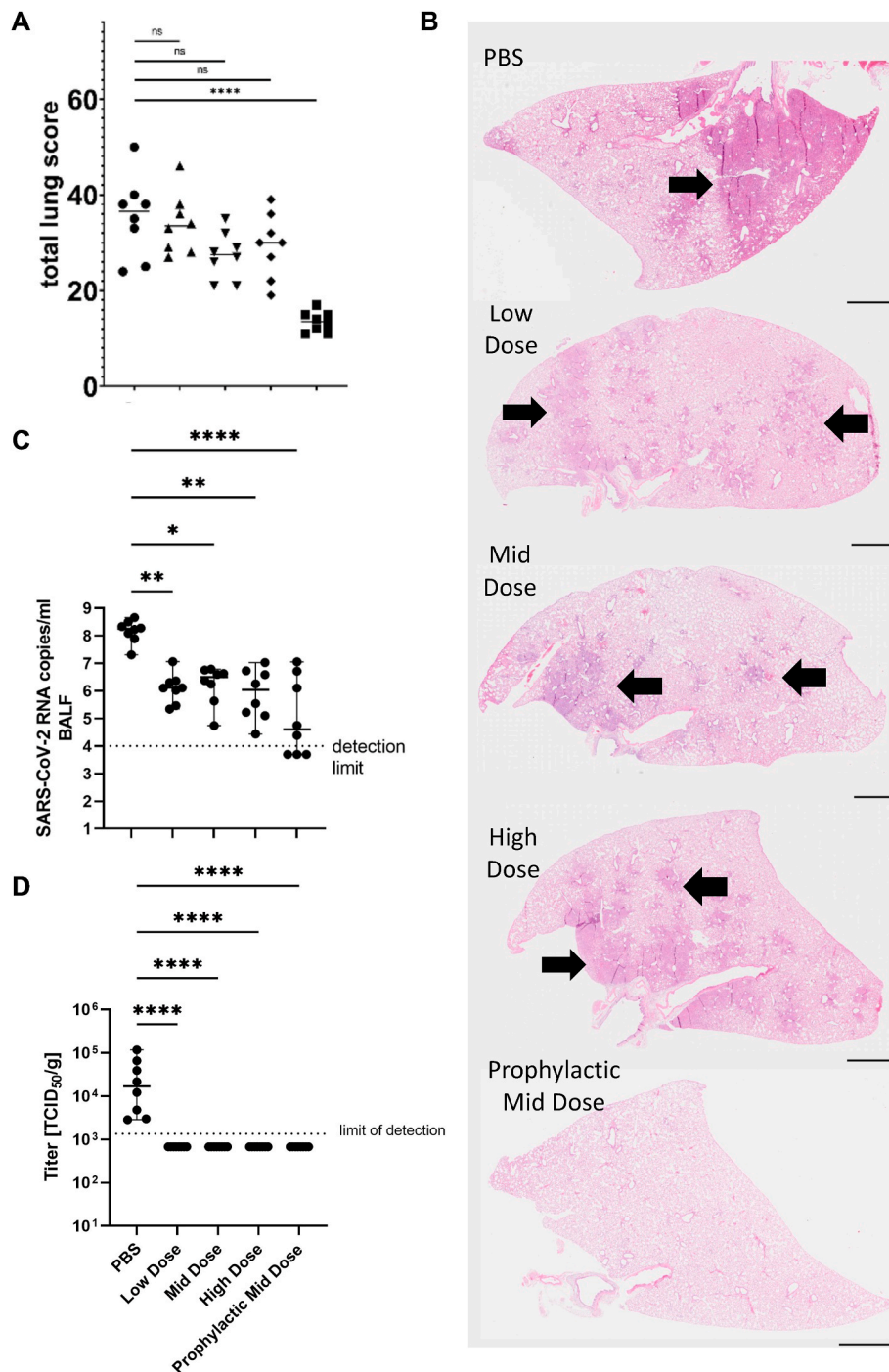


Fig. 9. Diminished virus replication and lung pathology upon inhalation of nanobody Re32D03. At day 6 after infection, the animals were euthanized and subjected to the following analyses. **A.** Morphological changes in VHH treated and SARS-CoV-2 infected hamsters. Dot plots display the total lung score of each animal with median scores as horizontal lines. Kruskal-Wallis test with subsequent Benjamini-Hochberg correction for multiple comparison; FDR: 0.05; ns: not significant; **** $p < 0.001$. **B.** Representative images of lung lesions show multifocal to coalescing consolidation in the PBS-treated and post-infection treated animals (arrows). Consolidation of lung tissue was characterized by inflammatory infiltrates and regeneration. Within the prophylactically treated group, only scattered foci of mild hypercellularity were detected. Lung overviews were taken from lungs representing the respective median score of each group. Bar: 2 mm. **C.** Quantification of SARS-CoV-2 RNA in bronchial lavage fluid (BALF). RNA levels were diminished significantly by prophylactic as well as therapeutic nanobody inhalation. **D.** Titers of infectious virus in the lungs, by median tissue culture infectious dose (TCID₅₀). Virus was found in all vehicle-treated animals but was undetectable in all nanobody-exposed animals.

When fully developed for clinical use, nanobodies could be self-inhaled in the absence of medical personnel and prescribed in an outpatient setting. It would be particularly useful upon unexpected exposure to the virus without proper face protection. Inhaling virus-

neutralizing nanobodies as soon as possible would greatly decrease the risk of infection. Given their long shelf-life, nanobody solutions could even be stored at home or otherwise at pharmacy shops for immediate availability in such events.

4. Materials and methods

4.1. Alpaca immunization, generation of the nanobody library and phage display selection

Three female alpacas, held at the Max Planck Institute for Multidisciplinary Sciences, had been immunized subcutaneously five times with the entire SARS-CoV-2 S1 domain (C-terminally His-tagged) as well as the Spike receptor-binding domain (RBD, C-terminally fused to the Fc region of human IgG1), both obtained from Sino Biological (sinobiological.com, 40591-V08H and 40592-V02H, respectively) (Güttler et al., 2021). The same three alpacas were immunized again with 200 µg of the stabilized wild-type (HexaPro) (Hsieh et al., 2020); and mutant (B.1.351/Beta (SinoBiologicals, 40591-V08H10), P.1/Gamma, B.1.427/Epsilon, P.3/Theta) SARS-CoV-2 Spike proteins. The generation of the nanobody library and phage display selection were performed essentially as described previously (Güttler et al., 2021; Pleiner et al., 2015), using biotinylated RBD as bait, at 30 pM concentration, and 50 mM Tris/HCl pH 7.5, 500 mM NaCl, 1% (w/v) BSA as a selection buffer. The Re30, 32 VHH series were obtained by three rounds of phage display against the RBD followed by one round against “tetra mutant” RBD (K417T, L452R, E484K, N501Y), in the presence of 100 nM unlabeled RBD-ACE2 fusion and with an off-rate selection step. The Ma6 series was obtained after another round of selection against the tetra mutant, pre-incubated with an Epitope 2 binder, Re5F10 (Güttler et al., 2021), in the presence of RBD-ACE2 competitor followed by an off-rate selection step. In off-rate selections, 100 nM competitors were added 20 min after mixing phages with bait, followed by retrieving phages after 18 h. A mixture of Epitope 1-Epitope 2 nanobody tandems (Güttler et al., 2021) and Re32B11/Re32D03 were used at 100 nM concentration for Re30-32 and Ma6 series selections, respectively. The alpaca Xenia was later immunized three times at different intervals with SARS-CoV-2 BA.1 Spike and RBD (C-terminally fused to the Fc region of human IgG1), with SARS-CoV-2 BA.2 Spike and with SARS-CoV-2 BA.5 Spike, respectively. The Ma28 series of nanobodies was obtained by two rounds of phage display against 1 nM and 300 pM BA.5 Spike, followed by one round against 300 pM BA.5 RBD. Recovered clones were identified by sequencing, and representatives of all classes were expressed as described below.

4.2. Periplasmic bacterial expression and purification of VHH antibody monomers

Nanobodies were expressed with an N-terminal DsbA1 signal sequence and a C-terminal His₁₂-tag in *E. coli* NEBExpress® (New England Biolabs). Cells were grown in TB medium (at 37 °C); protein expression was induced with 0.05 mM IPTG for 2 h. Bacteria were harvested by centrifugation and lysed by osmotic shock lysis (Mergulhão et al., 2005). Periplasmic extract was recovered by two consecutive centrifugation steps at 4 °C, first at 4000 g for 20 min (F13 rotor, Thermo Fisher Scientific) and then at 38,000 rpm for ~1 h (T647.5 rotor, Thermo Fisher Scientific). Soluble material was applied to a 1-ml Ni²⁺ chelate column. The matrix was washed with 50 mM Tris/HCl pH 7.5, 20 mM imidazole, 300 mM NaCl. The nanobodies were eluted with 50 mM Tris/HCl pH 7.5, 300 mM NaCl, 500 mM imidazole. Buffer was then exchanged to 50 mM Tris/HCl pH 7.5, 300 mM NaCl, 250 mM sucrose via a PD 10 desalting column (GE Healthcare). Aliquots were frozen in liquid nitrogen and stored at -80 °C.

4.3. Expression and purification of SARS-CoV-2 spike and free RBD

Expression and purification of Spike and RBDs were carried out as described (Güttler et al., 2021). For Spike expression, we used the SARS-CoV-2 S HexaPro construct Addgene #154754 (Hsieh et al., 2020), which comprises the Spike ectodomain (1–1208) with six exchanges to proline (F817P, A892P, A899P, A942P, K986P, V986P), a GSAS substitution at the furin cleavage site (residues 682–685), a C

terminal T4 foldon trimerization domain followed by a HRV 3C protease site, a His₈-tag and a Twin-Strep tag. P.1/Gamma, B.1.427/Epsilon, P.3/Theta Spikes were generated by site directed mutagenesis. For Omicron Spike proteins, clones of the respective spike sequences were obtained by gene synthesis (BA.1 Spike, GenScript, and BA.2 and BA.5, ThermoFisher). The constructs contained six stabilizing proline exchanges as well as furin cleavage site substitutions at positions analogous to the ones described above. We cloned them between the Acc65I/BamHI sites of the HexaPro construct to yield the identical C-terminal trimerization and purification tags.

Expi293F cells (10⁶ cells/ml, Thermo Fisher Scientific) were transiently transfected using Expifectamine and cultured for 6 days. Cultures were harvested by centrifugation. Supernatants were passed through a 0.22-µm filter, supplemented with buffer (1x PBS pH 7.4, 15 mM imidazole) and applied to Ni²⁺-chelate beads. Beads were washed with 50 mM Tris/HCl pH 8.0, 150 mM NaCl, 30 mM imidazole, and bound protein was eluted with buffer containing 500 mM imidazole. The eluate was then incubated with Strep-Tactin Sepharose resin (IBA), washed with 50 mM Tris/HCl pH 8.0, 150 mM NaCl and eluted with buffer supplemented with 50 mM Biotin. The protein was further purified on a Superose 6 10/300 column (GE Healthcare) equilibrated with 20 mM Tris/HCl pH 8.0, 150 mM NaCl.

For RBD expressions in mammalian cells, the SARS-CoV-2 Spike RBD (wt and mutants; residues 334–527) was clones into the pHL-avtag3 vector (Aricescu et al., 2006; Addgene, 99847), which provides a C-terminal Avi-His₆ tag. Expression and purification were performed as described for the Spike with some modifications. Cells were co-transfected with a BirA expression vector and cultured in the presence of 100 µg/ml D-biotin (Roth). Ni²⁺-chelate chromatography eluates were used in the BLI experiments without further purifications.

4.4. Kinetic measurements by bio-layer interferometry (BLI)

BLI experiments were performed using High Precision Streptavidin biosensors and an Octet RED96e instrument (ForteBio/Sartorius) at 25 °C with Phosphate-Buffered Saline (PBS) pH 7.4, 0.02% (w/v) Tween 20 and 0.1% (w/v) BSA as assay buffer. Biotinylated RBDs (50 nM) were immobilized on biosensors for 150 s (corresponding to 1–1.2 nm wavelength shift/binding signal change). Subsequently, the biosensors were dipped into wells containing ligands 450 s for association, and then incubated 30 min with assay buffer for dissociation. Data were reference-subtracted, and curves were fitted with a mass transport model (Octet Data Analysis HT 12.0 software). For wildtype RBD measurements, the biosensors were incubated with 40, 20, 10, 5, 2.5, or 1.25 nM nanobody. For RBD mutants, the biosensors were incubated with 20, 6.66, and 2.22 nM nanobody.

4.5. ACE2 competition experiments

Biotinylated Human ACE2 (10108-H27B-B, Sino Biological) was immobilized on biosensors until a 0.5 nm wavelength shift/binding signal was reached. Biosensors were dipped into wells containing 100 nM RBD and 500 nM VHHs for 240 s.

4.6. Differential scanning fluorimetry (DSF/thermoFluor)

Nanobodies were diluted to 1 mg/ml in 20 µl 50 mM Tris/HCl pH 8.0, 300 mM NaCl, 1x SYPRO Orange (Life Technologies). Samples were pipetted into a Hard-Shell® 96-well plate (Bio-Rad). The plate was sealed with transparent MicroSeal® ‘B’ Seal (Bio-Rad) and briefly centrifuged to remove air bubbles. Experiments were performed using the CFX96 Real-Time System (C1000 Thermal Cycler, BioRad). The samples were incubated for 5 min at 20 °C before the temperature was gradually increased to 95 °C with 1K-increments and 45 s for each incubation step. At the end of each step, the SYPRO Orange fluorescence was measured using the HEX channel. Melting temperatures are defined

as the inflection point of the melting curve before reaching the first melting peak. Nanobody variants were considered stable if they produced no melting peak.

4.7. Preparation of complexes for crystallization

The wild-type (Wuhan) SARS-CoV-2 receptor-binding domain (WT RBD, spike protein S1 residues 334–526, N343D) was co-expressed with His₁₄-BdNEDD8-tagged VHHs Re21D01 or Re21H01. VHH Re30H02 was expressed in an untagged form in *P. pastoris* BG11 (ATUM)-derived strains, constructed as described (Wu and Letchworth, 2004), for 48 h by methanol induction at 30 °C in Buffered Methanol-complex Medium (BMMY). Cells were pelleted by centrifugation at 3000g (5 min), and the culture supernatant was then buffered with Tris/HCl pH 8.0 and used for ternary complex assembly.

VHHs Ma6F06 and Re32D03 were produced in an untagged form in *P. pastoris* by bioreactor fermentation. The culture supernatants were deionized and adjusted to pH 7.5 (Ma6F06) or 8.0 (Re32D03) with Tris/HCl. The VHHs were purified by anion-exchange chromatography (Q Sepharose Fast Flow, with 10 mM Tris/HCl pH 7.0 (Ma6F06) or 7.5 (Re32D03) for binding and elution with a NaCl gradient to 150 mM (Ma6F06) or 1 M (Re32D03). The VHHs were then used for ternary complex assembly (see below).

BA.2.75-like SARS-CoV-2 receptor-binding domain (BA.2.75-like RBD, spike protein S1 residues 333–517, N343D) was co-expressed with His₁₄-BdNEDD8-tagged VHH Ma3B12 in *E. coli* SHuffle Express (New England Biolabs). Cells were grown in Terrific Broth (TB) medium, and protein expression was induced at 21 °C with 0.135 mM IPTG. Six hours after induction, 10 mM EDTA was added to the culture medium. The bacteria were then pelleted, resuspended in 50 mM Tris/HCl pH 7.5, 20 mM imidazole, 500 mM NaCl and frozen in liquid nitrogen. Cells were lysed by thawing and sonication, and insoluble material was removed by ultracentrifugation at 160,000 g (4 °C, 1 h, rotor T647.5, Thermo Fisher Scientific). The soluble lysate was used for ternary complex assembly.

The ternary complexes were assembled and purified by Ni²⁺-chelate affinity chromatography, by immobilizing the H₁₄-tagged components and supplying the untagged ones in molar excess, with subsequent protease elution using BdNEDP1 protease (Frey and Görlich, 2014), and size exclusion chromatography (HiLoad 16/600 Superdex 75, Cytiva, equilibrated to 20 mM Tris/HCl pH 7.5, 150 mM NaCl, 5% (v/v) glycerol for complexes with VHHs Re21H01 and Ma3B12). Complexes were then used directly for crystallization.

4.8. Crystallization of ternary complexes of RBDs and nanobodies

All complex preparations (at 10–15 mg/ml protein concentration) were screened by sitting drop vapor diffusion (100 nl protein +100 nl reservoir). The crystallization and the cryo-protection conditions for the crystals used for solving the structures are provided in the following table.

Complex	Crystallization condition	Cryo-protection condition
WT RBD- Re21D01- Re30H02-	25% (w/v) PEG smear broad, 50 mM arginine, 50 mM MSG, 5% glycerol	28% PEG smear broad, 50 mM arginine, 50 mM MSG, 15% (v/v) glycerol
WT RBD- Re21H01- Ma6F06	100 mM sodium citrate pH 4.5, 20% (w/v) PEG 4000	100 mM sodium citrate pH 4.5, 20% (w/v) PEG 4000, 20% (v/v) glycerol
BA.2.75i RBD- Ma3B12- Re32D03	100 mM HEPES pH 7.0, 20% (w/v) PEG 8000	100 mM HEPES pH 7.0, 20% (w/v) PEG 8000, 15% (v/v) glycerol
BA.1 RBD- Ma3F05- Ma16B06	100 mM HEPES pH 7.8 20% (v/v) PEG smear high, 150 mM lithium sulphate, 5 mM magnesium chloride	100 mM HEPES pH 7.8 20% (v/v) PEG smear high, 150 mM lithium sulphate, 5 mM magnesium chloride 15% (v/v) glycerol

4.9. Structure determination

All diffraction data were collected at beamline PXII-X10SA at the Swiss Light Source (SLS, Paul-Scherrer-Institut, Villigen, Switzerland) at 100 K, using an EIGER2 X 16M detector (DECTRIS). The datasets were processed in XDS (Kabsch, 2010) and the Phenix Package (Liebschner et al., 2019) was used for structure solving. The structures were solved by molecular replacement (MR) in PHASER (McCoy, 2007), using published RBD and nanobody (Re5D06) models (PDB IDs 7OLZ and 7ON5) (Güttler et al., 2021) for searches. For the nanobody search models, CDR loops were removed. Model building was performed with the Phenix AutoBuild Wizard (Terwilliger et al., 2008) and/or manually in Coot (Emsley et al., 2010), followed by iterative cycles of refinement in Phenix.refine (Afonine et al., 2012) until convergence at the final models (Suppl. Table 6).

For MR of the Re30H02-RBD-Re21D01 complex, searches with two copies of the RBD were followed by four copies of nanobody. The RBD-Re21D01 model created from this complex was used as an MR search model for the Ma6F06-RBD-Re21H01 complex, in conjunction with nanobody searches for Ma6F06. MR of the Re32D03-Omicron BA.2.75 RBD-Ma3B12 complex was performed with an Omicron BA.2.75 RBD model, created in SWISS-MODEL (Waterhouse et al., 2018) and two nanobodies as search models. Similarly, MR of the Ma16B06•Omicron BA.1 RBD•Ma3F05 complex was performed with an Omicron BA.1 RBD model and two nanobodies as search models.

The quality of all final models was assessed with MolProbity (Williams et al., 2018). The structures were analyzed with PyMOL (The PyMOL Molecular Graphics System v.2.1, Schrödinger, LLC) and UCSF Chimera (Pettersen et al., 2004). Figures were prepared using UCSF Chimera.

4.10. Sample preparation for cryo-EM, grid freezing and screening

Purified SARS-CoV-2 BA.1 Spike and VHH Ma16B06 were incubated in a 1:9 M ratio (RBD:nanobody ratio of 1:3) and subjected to size exclusion chromatography (Superose 6 Increase 3.2/300, Cytiva; equilibrated with 2 mM Tris/HCl pH 8.0, 150 mM NaCl). A Vitrobot Mark IV (FEI Company) was used for grid preparation: 3 µl of the complex peak fraction (2.0 mg/ml) was applied to a freshly (air) glow-discharged Quantifoil UltrAuFoil R2/2 grid (200 mesh). The grid was blotted for 3 s at 4 °C and 95% humidity with a blot force of 5 and then plunge-frozen in liquid ethane.

4.11. Cryo-EM data collection and processing

Data were collected with SerialEM (Mastrorade, 2005) using a Titan Krios G2 TEM (Thermo Fisher Scientific) operated at 300 kV, equipped with a Gatan GIF Quantum LS energy filter and a Gatan K3 Summit detector (operated in counting mode, non-super-resolution). Details are shown in Suppl. Table 7. We obtained 7592 movies corresponding to four movies per imaged hole (beam-image-shift).

Warp 1.0.9 (Tegunov and Cramer, 2019) was used (in parallel to data acquisition) for motion correction, dose weighting, CTF estimation and particle picking. Particles were extracted in RELION 3.1 (Zivanov et al., 2018) at 4.2 Å/pixel (4x binned) with a box size of 84 pixels and subjected to 2D and 3D classification (Suppl. Fig. 11). A reference volume from a smaller screening dataset was used for 3D classification. The complete data processing workflow is summarized in Suppl. Fig. 11. Map post-processing was performed in RELION with tight masking. See Suppl. Fig. 11 for details. The FSC curve and local resolution plot are shown in Suppl. Fig. 12.

Docking of the RBD-Ma16B06 crystal structure: The crystallographic model of the BA.1 RBD-Ma16B06 complex was rigid body-docked into the cryo-EM map using UCSF Chimera (Pettersen et al., 2004), followed by one round of refinement in PHENIX (Afonine et al., 2012) and a small number of side chain rotamer adjustments in Coot (Emsley et al., 2010).

4.12. Virus neutralization assays

The following SARS-CoV-2 variants were investigated as to their neutralization by nanobodies:

Virus strain	Source	Identifier
SARS-CoV-2 'wildtype', Göttingen/Germany	Isolated in our lab (Stegmann et al., 2021)	N/A
SARS-CoV-2 Alpha (B.1.1.7)	Robert Koch Institute (Berlin, Germany)	EVA: 009V-05245
SARS-CoV-2 Delta (B.1.617.2)	Robert Koch Institute	EVA: 009V-04187
SARS-CoV-2 Omicron (BA.1.17)	Isolated in our lab (Feb 2022)	EPI_ISL_18421902
SARS-CoV-2 Omicron (BA.5)	Robert Koch Institute	EVA: 009V-05261

VeroE6 cells (Vero C1008) were cultured in DMEM (with Gluta-MAX™, Gibco) medium containing 10% FBS (Merck), 50 units/mL Penicillin, 50 µg/mL Streptomycin (Gibco), 10 µg/mL Ciprofloxacin (Bayer) and 2 µg/mL Tetracycline (Sigma), and maintained at 37 °C in a humidified chamber with 5% CO₂.

For virus-nanobody neutralization assays, 3500 cells were seeded per well in a 96-well plate (Zell-Kontakt, 3241-20). 24 hrs later, the medium was changed to a 2% FCS medium. 2x dilutions of nanobody were also prepared (10 nM–0.034 nM) in 2% FCS medium. ~220 FFU of each virus stock were added to all nanobody dilutions (1:1 vol), and the mixture was incubated for 1–2 h at 37 °C while shaking the plate every 10 min. Afterwards, 100 µL of the virus-nanobody mix was added to the VeroE6 cell monolayer and incubated for 48 h at 37 °C.

4.13. Virus RNA quantification by RT-PCR

100 µL virus supernatant from each treatment condition was inactivated with 100 µL GTC buffer (MagNA Pure LC Total Nucleic Acid Isolation Kit, Roche), and viral RNA was isolated using Trizol LS, phenol and chloroform extraction. The RNA pellet was washed with 75% ethanol, dried and dissolved in nuclease free water.

RNA was quantified using quantitative RT-PCR with a TaqMan Probe (Corman et al., 2020), using the following oligonucleotides, to amplify and detect a region (26,141–26,253) in the SARS-CoV-2 genome encoding the envelope protein.

Primer	5' – Sequence – 3'	Modification
F (forward)	ACAGGTACGTTAATAGTTAATAGCGT	–
R (reverse)	ATATTGCAGCAGTACGCACACA	–
P (probe)	ACACTAGCCATCCTTACTGCGCTTCG	5' FAM, 3' BbQ

4.14. Immunofluorescence detection of infected cells

48 h post infection of Vero E6 cells in 96-well plates, the cells were fixed with 4% paraformaldehyde (Sigma) in PBS. Immunofluorescence analysis and imaging was carried out essentially as described (Güttler et al., 2021). Briefly, the cells were permeabilized using 0.15% Triton-X-100 in PBS, blocked with 5% BSA in PBS, and stained with a pool of anti-Spike protein nanobodies, coupled to Alexa 488, while the nuclei were counterstained with 4',6-diamidino-2-phenylindole (DAPI). The number of infected cells were counted using a macro on ImageJ (1.53k/Java-1.8.0.172), which converts the image to an 8-bit format and inverts the image to obtain dark spots in place of A488 or DAPI fluorescent signals. The number of such spots were counted by setting a suitable threshold. The percentage of infected cells were calculated by dividing the number of A488 spots with the number of DAPI spots and multiplying by 100.

4.15. Pseudotyped VSV for neutralization assays

HEK293T cells were used for preparation of pseudotyped Vesicular

Stomatitis Virus (VSV). The cells were maintained in DMEM supplemented with 10% FBS (Merck), Glutamine, 50 units/mL Penicillin (Gibco), 50 µg/mL Streptomycin (Gibco), 10 µg/mL Ciprofloxacin (Bayer), and 2 µg/mL Tetracycline (Sigma), at 37 °C in a humidified chamber with 5% CO₂.

3,800,000 HEK293T cells were seeded in 15 cm-plates. After 24 h, the cells were transfected with expression plasmids for SARS-CoV-2 (or variant) spike proteins, (SinoBiologicals, Virongy), using Lipofectamine3000 (Life technologies). Upon another 24hrs, the transfected cells were infected with VSV-ΔG-GFP/Fluc-G virus particles (Zimmer et al., 2014), provided by the team of Stefan Pöhlmann (German Primate Center, Göttingen), with generous permission by Gerd Zimmer (IVI, Bern, Switzerland), at MOI 2 for 2 h. Then, the medium was replaced with medium containing 500 ng/mL anti-VSV-G antibody (Kerafast) to neutralize background VSV-ΔG-GFP/Fluc-G particles. After another 24 h at 37 °C, the supernatant with VSV-ΔG-GFP/Fluc-S pseudotype virus was harvested, and cell debris was spun down at 2000 g for 10 min.

The pseudotypes were then directly combined with nanobody dilutions (0.1 nM–100 nM) in 96-well plates and incubated at 37 °C for 2 h. The mixtures were then added to Vero E6 cell monolayers (seeded at 5000 cells per well in 96-well plates, Greiner). The following day, all infected (GFP-positive) cells were identified using a Celigo Image cytometer (Nexcelom), and the number of infected cells were counted using ImageJ (1.53k/Java-1.8.0.172).

4.16. Large-scale production of nanobodies

The production scheme is summarized in Suppl. Fig. 3. A *Pichia pastoris* strain for high-yield secretion of nanobody into the culture medium was constructed essentially as described (Güttler et al., 2021; Wu and Letchworth, 2004). The production was carried out in Modified Basal salt medium (BSM): CaCl₂ 3.4 mM, H₃PO₄ 85% 13.5 mL/L, MgSO₄ 30.4 mM, K₂SO₄ 51.6 mM, KOH 35.6 mM, Glycerol 434 mM, Citric acid 20 mM, (NH₄)₂SO₄ 75.6 mM, NaCl 4.2 mM, PTM1 4.35 mL/L, Antifoam (polypropylene glycol P 2000) 0.1 mL/L, Biotin 818 nM, CuSO₄ 24 mM, KI 542 nM, MnSO₄ 18.5 mM, Na₂MoO₄ 826 nM, H₃BO₃ 323 nM, CoCl₂ 723 nM.

The fermentation process was carried out first in the AMBR250 system (Sartorius), followed by small-scale bench-top fermenters (2L & 5L), and then a mid-size-scale expression that was carried out in a 30L-fermenter (both Sartorius). The cultivation process was based on glycerol feeding to gain initial biomass, followed by methanol feeding. The process duration was 120 h with a yield of 3 g/L. The broth was centrifuged at 17600 g for 15 min. For purification of the protein at a sterile grade, we divided the process as follows: clarification of the harvested broth, purification using two columns, buffer exchange and concentration by an Ultrafiltration/Diafiltration (UFDF) system (Sartorius). Following the harvest, the broth was filtered to reach sterile-grade filtration. To prepare the protein for further purification, we used a UFDF process to reduce salt concentration, and then the protein was captured on an AIEC (ion exchange) column. The UFDF process was re-applied as a final purification step to reach high concentration and buffer exchange suitable for formulation.

4.17. Pharmacokinetics of nanobodies

The study was performed in compliance with the Israel Animal Welfare Act and following the Israel Board for Animal Experiments Ethics Committee approval NPC-Sc- IL-2206-132-4.

The nanobody was administered intratracheally at 2.7 mg/kg to male Sprague Dawley rats. At 0.5, 1, 2, 6, 10 and 24 h post inoculation, each group (n = 3/time point) was euthanized. The lungs were removed and washed with cold PBS supplemented with 1% (v/v) protease inhibitor cocktail (Thermo Fisher cat no. 78425). The collected lavage fluid was centrifuged (7 min at 400g, 4 °C). The resulting Bronchoalveolar Lavage (BAL) supernatant was analyzed for nanobody

content using the Octet R8 Biolayer Interferometry (BLI) system. For this purpose, High Precision Streptavidin (SAX) Biosensors were coated with biotinylated Receptor Binding Domain (RBD) from the Wuhan Spike protein (Sino Biological CAT#40592-V27H-B). Then, the pre-coated Biosensors were mixed with the BAL samples with constant agitation at 30 °C to allow the VHH binding. The binding rates were calculated against a linear nanobody standard curve in a range of 0.625–40 µg/ml. Each BAL sample was tested using two independent dilutions with the diluent 1% BSA in PBS, in order to verify the absence of matrix effects. The analysis was performed using noncompartmental analysis (NCA) using the PKSolver software (Zhang et al., 2010).

4.18. Aerosol preparation

The inhalation system is depicted schematically in Fig. 8A and photographically in Suppl. Fig. 6A. It consisted of a pressurized dispersion nozzle (atomizer, FhG-ITEM, own development) connected to a mixing chamber positioned upstream of the left inlet of a horizontal flow exposure chamber with a volume of 1 m³. The nanobody solutions were fed into the nozzle and dispersed by pressurized air into the mixing chamber. Air was sucked through an inlet filter into the mixing chamber and the aerosol then through the exposure chamber. This procedure resulted in a negative pressure in the entire system and thus prevented leakage of the active ingredient. Cages within the chamber were housing 3 hamsters each.

To verify a constant and homogeneous aerosol in the exposure chamber, comprehensive measurements downstream of the cages were conducted, determining aerosol concentration and particle size distribution using a Marple cascade impactor. Aerosol concentrations were additionally monitored continuously by photometry. Moreover, filter samples were taken twice per day to measure the actual concentration by gravimetry. Particle size measurements were conducted at least twice during for each dose group.

4.19. Animal model of SARS-CoV-2 infection

The animal experiment was conducted under biosafety level 3 (BSL-3) conditions, in compliance with the European and national regulations for animal experimentation (European Directive, 2010/63/EU; Animal Welfare Acts in Germany) and Animal Welfare Act, approved by the Niedersächsisches Landesamt für Verbraucherschutz und Lebensmittelsicherheit (LAVES, Lower Saxony, Germany; reference number: 33.19-42502-04-22-00154). For SARS-CoV-2 challenge infection, animals were housed in ventilated cages individually (IVCs, IsoRat 900N, Tecniplast) at the Research Center for Emerging Infections and Zoonoses (RIZ), University of Veterinary Medicine, Hannover, Germany.

Male Syrian golden hamsters (10 week-old, *Mesocricetus auratus*; breed HsdHan®: AURA) were purchased from Janvier-Labs (France) and were kept under standard housing conditions (21 ± 2 °C, 40–50% humidity, food and water ad libitum) with a 12:12 light–dark cycle.

For infection, hamsters at the age of 9–14 weeks were anesthetized by inhalation of isoflurane (4–1.5% total volume) for 2 min (Baxter, United States). Infection was performed by intranasal application of virus solution in 100 µl DMEM with 2 % fetal bovine serum. We infected the hamsters with 1×10^4 TCID₅₀ units of SARS-CoV-2 (isolate Germany/BavPat1/2020). Clinical symptoms, including bodyweight loss, cardiovascular function, respiratory symptoms, and body conditions were monitored daily over 6 days post infection (p.i.) according to a scoring system (Suppl. Fig. 7A).

Animals were trained for being in the inhalation chamber, without aerosol, twice daily for 5 days prior to the start of the inhalation of the substance (15 min, 30 min, 60 min, 90 min and 120 min consecutively). Inhalations were then conducted in the inhalation chamber, for 120 min. Animals were observed and scored for activity and health condition during the entire training or inhalation time.

For all inhalation experiments, animals were allowed to inhale the

52 ml of the relevant dose (Suppl. Fig. 7B) of the sprayed substance for 2 h, twice daily for 5 days. Hamsters were divided into groups according to the nanobody concentrations, and each group included 8 hamsters. The position of the individual hamster in the inhalation chamber was systematically exchanged during the experiment.

During the 5 days of inhalation, data were recorded from photometer during the whole inhalation period to ensure the stability of nebulization. In addition, gravimetry and impactor samples were acquired to determine the aerodynamic particle size distributions. Gravimetry and impactor samples were screened for 600 and 60 s, respectively, except for the low dose group where impactor samples were taken at a frequency of 180 s. Gravimetry samples were collected during every inhalation (mornings and evenings, 10 times), whereas impactor samples were taken 3 times. The timeline of animal infection and treatment is depicted in Suppl. Fig. 7.

On day 6 p.i., all hamsters were euthanized by applying an overdosed intra-peritoneal injection of Ketamin-Medetomidin solution in sterile sodium chloride (100 mg/ml Ketamidol®, WDT, Garbsen, Germany; 1 mg/ml Domitor®, Orion-Pharma, Ismaning, Germany) with a dose adjusted to the individual body weight (1000 mg/kg Ketamin, 1,25 mg/kg Medetomidin).

Virus stock preparation. SARS-CoV-2 (human 2019-nCoV isolate Germany/BavPat1/2020, provided by Christian Drosten, Charité, Berlin, Germany, through the European Virus Archive—Global/EVAg Ref-SKU: 026V-03883) was passaged once on Vero E6 cells (ATCC #CRL-1586) in Dulbecco's Modified Eagle's Medium (DMEM, Sigma-Aldrich GmbH) supplemented with 2 % fetal bovine serum at 37 °C. The virus was pooled, aliquoted and stored at –80 °C until usage. Virus titers of stock solutions were determined by virus titration on Vero E6 cells as described below ('Virus titration').

Necropsy and Pathology. At the day of necropsy, oropharyngeal swabs were collected with FloqSwabs (# 80501CS, Typ 501CS01, Mast Diagnostica GmbH) and stored in 1 ml of medium (DMEM and 2% FBS). EDTA-blood and Serum samples were collected intracardially. Bronchoalveolar lavage fluid (BALF) was collected with an 18-gauge needle (1.2 × 4 mm, Sterican) by injection of 1 ml phosphate buffered saline (PBS) directly in the gorge part of the trachea and consecutive aspiration of approximately 0.6 ml fluid.

The left lung lobe was collected and pre-fixed by injection of 10% neutral buffered formalin (NBF, VWR International GmbH, Hannover, Germany) for optimal histopathological morphology (Meyerholz et al., 2018). Thereafter, 2–3 µm sections were routinely stained with hematoxylin-eosin for histopathological evaluation. Lesions were scored semiquantitatively by two pathologists (WR, WB) according to established scoring systems (Armando et al., 2022). In summary, a 4-tier-scoring system for alveolar, conductive airways and vascular lesions was applied. For final scores, extent, and severity of tracheal, airway and alveolar lesions were multiplied before summing of all scores.

Final scores of all groups were compared by Kruskal-Wallis test with subsequent pairwise Mann-Whitney-U-tests and Benjamini-Hochberg correction for multiple comparisons (False Detection Rate: 0.05) by GraphPad Prism software for Windows™ (GraphPad Software, San Diego, CA, USA). Statistically significant differences between groups were assumed at exact p-values ≤ 0.05. For image preparation, hamster lungs resembling the median score of each group were selected and digitalized with the Olympus VS200 slide scanner (Olympus Deutschland GmbH, Hamburg, Germany).

The right cranial lung lobe was collected in micro screw tubes (2 ml, 72.694.005, Sarstedt) with 500 µl DMEM and a 5 mm stainless steel bead (69989, Qiagen) for tissue homogenization and subsequent end-point dilution analyses and SARS-CoV-2-specific PCR (see sections 'virus titration' and 'SARS-CoV-2 RT-qPCR').

Virus titration. The SARS-CoV-2 titres in lung homogenates were quantified by end-point dilution assays. At the day of necropsy, lung tissue of the size of a grain of rice was collected in micro screw tubes (Sarstedt) containing 500 µl DMEM. Each lung tissue piece was

homogenized with a 5 mm steel bead (Qiagen) using a TissueLyser II (Qiagen) at 24 Hz for 1 min in pre-cooled racks (4 °C), centrifuged at maximum speed for 1 min at 4 °C and immediately frozen at –80 °C. One day prior to the end-point dilution assay, 180 µl of Vero E6 cell suspension were seeded at a density of 1×10^5 cells/ml in growth medium (DMEM, 2% FBS) into a 96 well tissue culture plate for adherent cells (83.3911.002, Sarstedt). For titration, 20 µl of lung homogenate supernatant per well were used for a 1:10 dilution series with each sample being tested in quadruplicate according to (Smither et al., 2013). After incubation at 37 °C, 5 % CO₂, the cytopathic effect (CPE) was evaluated with a binocular light microscope (Primover KMAT, Zeiss) at 5 dpi. Titres of samples that showed CPE in 1–4 wells at the detection limit (first row of 96 well plate) were set to the detection limit ($1,76 \times 10^2$), while data points of samples without detectable CPE were set to half of the detection limit ($8,8 \times 10^1$) to allow statistical analysis, as described previously (Meyer zu Natrup et al., 2022). Virus titres are given as 50% tissue culture infective dose per millilitre (TCID₅₀/ml) and are calculated according to the Spaerman-Kaerber method (Kärber, 1931). For this analysis, the following TCID₅₀-calculator was used: <https://www.klinikum.uni-heidelberg.de/zentrum-fuer-infektiologie/molecular-virology/welcome/downloads/>. Finally, the data were also calculated as TCID₅₀ relative to g tissue in 500 µl volume of each sample.

SARS-CoV-2-RNA extraction and quantification. SARS-CoV-2-RNA was extracted and quantified as described previously (Ciurkiewicz et al., 2022). Briefly, RNA was extracted from 100 µl of lung homogenate supernatant, BALF or swab fluid and eluted in 100 µl eluate buffer using the magnetic bead-based NucleoMag Vet Kit (Macherey-Nagel) at a KingFisher 96 instrument (ThermoFisher). For SARS-CoV-2-RNA detection, 2.5 µl of eluate was amplified with the AgPath-ID One-Step RT-PCR Reagents kit (4387391, ThermoFisher) at a CFX 96 real-time cycler (Bio-rad). The SARS-CoV-2-RNA copy number in each sample was quantified using the primer-probe assay and PCR standard IP4 from Institut Pasteur and verified with an internal control system (EGFP-Mix1) as described previously (Ciurkiewicz et al., 2022; Hoffmann et al., 2006; Schulz et al., 2021). The copy number of each sample was calculated per gram (g) according to the weight of the lung tissue piece in the respective sample tube. The detection limit of the PCR assay are 10 SARS-CoV-2-RNA copies/µl. The detection limit for RNA copies/g (7.6×10^4 copies/g) was calculated with the mean of all lung tissue weights (0.0659 g). Copy numbers of negative samples are given as half of the detection limit (3.8×10^4 copies/g) to allow statistical analysis. All statistical analyses were conducted with GraphPad prism (version 9.0.0). Results of nanobody-treated groups were compared with the mock-treated group (PBS) with Kruskal-Wallis test for non-normally distributed data points.

Hematology. EDTA-blood samples were analyzed automatically at a hematology instrument (Vet abc plus, Scilvet). The instrument differentiates erythrocytes, platelets and leukocytes, the latter including lymphocytes, monocytes, neutrophil and eosinophil granulocytes. Furthermore, the mean corpuscular volume (MCV), mean corpuscular hemoglobin (MCH), and mean corpuscular hemoglobin concentration (MCHC) of erythrocytes, the hematocrit and the mean platelet volume (MPV) are determined. Cellular components are measured by impedance and the hemoglobin concentration by photometry. As additional control, EDTA-blood from 3 uninfected hamster with the same age and sex were used to be compared with the animals of the 5 treatment groups. The blood harvest was done from animals in compliance with the European and national regulations for animal experimentation (European Directive, 2010/63/EU; Animal Welfare Acts in Germany) and Animal Welfare Act, approved by the local animal welfare officer (reference number: TiHo-T-2022-12, University of Veterinary Medicine Hannover, Germany). Statistical analyses and data visualization were conducted with GraphPad Prism (version 9.5.0). Outliers were identified with the ROUT method and excluded from further analysis (Motulsky and Brown, 2006). Nanobody-treated groups and the control group were statistically compared to the mock (PBS)-treated group. Ordinary

one-way ANOVA and Kruskal-Wallis test were conducted for normally and non-normally distributed data points, respectively.

Blood chemistry. Serum samples from hamsters were analyzed with the Fuji Dri-Chem Nx500i (Fujifilm). The dry chemistry generally analyses parameters with a colorimetric method using a spectrophotometer, except for electrolytes. The electrolytes sodium, potassium and chloride are measured together with a reference solution (Fluid RE, Fujifilm) with a potentiometer. Similar to hematology, EDTA-blood from 3 uninfected hamster with the same age and sex were used to be compared with the animals of the 5 treatment groups as additional control.

CRediT authorship contribution statement

Metin Aksu: Investigation, Methodology, Writing – original draft, Writing – review & editing. **Priya Kumar:** Investigation, Methodology, Writing – review & editing. **Thomas Güttler:** Data curation, Investigation, Methodology, Software. **Waltraud Taxer:** Investigation, Methodology. **Kathrin Gregor:** Investigation, Methodology. **Bianka Mußil:** Investigation, Methodology. **Oleh Rymarenko:** Investigation, Methodology. **Antje Dickmanns:** Investigation, Methodology. **Sabrina Gerber:** Investigation, Methodology. **Wencke Reineking:** Investigation, Methodology. **Claudia Schulz:** Investigation, Methodology. **Timo Henneck:** Investigation, Methodology. **Ahmed Mohamed:** Investigation, Methodology. **Gerhard Pohlmann:** Investigation, Methodology, Supervision. **Mehmet Ramazanoglu:** Investigation, Methodology. **Kemal Mese:** Investigation, Methodology, Methodology. **Uwe Groß:** Supervision. **Tamar Ben-Yedidia:** Investigation, Methodology, Supervision. **Oded Ovadia:** Investigation, Methodology. **Dalit Weinstein Fischer:** Methodology. **Merav Kamensky:** Methodology. **Amir Reichman:** Investigation, Supervision. **Wolfgang Baumgärtner:** Investigation, Methodology, Supervision. **Maren von Köckritz-Blickwede:** Investigation, Methodology, Supervision. **Matthias Döbelstein:** Conceptualization, Funding acquisition, Investigation, Methodology, Project administration, Supervision, Writing – original draft, Writing – review & editing. **Dirk Görlich:** Conceptualization, Data curation, Formal analysis, Funding acquisition, Investigation, Methodology, Project administration, Supervision, Writing – original draft, Writing – review & editing.

Declaration of competing interest

The authors declare the following financial interests/personal relationships which may be considered as potential competing interests: The following authors are employees of Scinai Immunotherapeutics Ltd., a company dedicated to developing Nanobodies for clinical use. Tamar Ben-Yedidia, Oded Ovadia, Dalit Weinstein Fischer, Amir Reichman. Moreover, Matthias Döbelstein is a member of the scientific advisory board of Scinai Immunotherapeutics Ltd..

Data availability

The coordinates and structure factors have been deposited with the Protein Data Bank (PDB, <https://www.rcsb.org/>) with accession codes 8Q93 (Re30H02•RBD•Re21D01), 8Q94 (Re32D03•Omicron BA2.75 RBD•Ma3B12), 8Q7S (Ma6F06•RBD•Re21H01), and 8Q95 (Ma16B06•Omicron BA.1 RBD•Ma3F05). The cryo-EM reconstructions were deposited with the Electron Microscopy Data Bank (EMDB, <https://emdb-empair.org/>) under accession codes EMD-18941 (Omicron BA.1 Spike•Ma16B06 complex "body002").

Acknowledgements

We thank G. Zimmer for very helpful advice on pseudotyped VSV, the crystallization and the cryo-EM facilities of the MPI-NAT for splendid support, Christian Dienemann for help with cryo-EM data collection and data processing, the staff of synchrotron beamlines at the

Swiss Light Source (Villigen, X10SA, PXII) for assistance during data collection. This work was funded by the Volkswagenstiftung, 9A827 to MD and DG.

Appendix A. Supplementary data

Supplementary data to this article can be found online at <https://doi.org/10.1016/j.antiviral.2023.105778>.

References

- Abdiche, Y., Malashock, D., Pinkerton, A., Pons, J., 2008. Determining kinetics and affinities of protein interactions using a parallel real-time label-free biosensor, the Octet. *Anal. Biochem.* 377, 209–217. <https://doi.org/10.1016/j.ab.2008.03.035>.
- Afonine, P.V., Grosse-Kunstleve, R.W., Echols, N., Headd, J.J., Moriarty, N.W., Mustyakimov, M., Terwilliger, T.C., Urzhumtsev, A., Zwart, P.H., Adams, P.D., 2012. Towards automated crystallographic structure refinement with phenix.refine. *Acta Crystallogr D Biol Crystallogr* 68, 352–367. <https://doi.org/10.1107/S0907444912001308>.
- Ahmad, J., Jiang, J., Boyd, L.F., Zeher, A., Huang, R., Xia, D., Natarajan, K., Margulies, D. H., 2021. Structures of synthetic nanobody-SARS-CoV-2 receptor-binding domain complexes reveal distinct sites of interaction. *J. Biol. Chem.* 297, 101202 <https://doi.org/10.1016/j.jbc.2021.101202>.
- Arbabi Ghahroudi, M., Desmyter, A., Wyns, L., Hamers, R., Muyldermans, S., 1997. Selection and identification of single domain antibody fragments from camel heavy-chain antibodies. *FEBS Lett.* 414, 521–526. [https://doi.org/10.1016/S0014-5793\(97\)01062-4](https://doi.org/10.1016/S0014-5793(97)01062-4).
- Ari, A., Fink, J.B., 2020. Recent advances in aerosol devices for the delivery of inhaled medications. *Expet Opin. Drug Deliv.* 17, 133–144. <https://doi.org/10.1080/17425247.2020.1712356>.
- Aricescu, A.R., Lu, W., Jones, E.Y., 2006. A time- and cost-efficient system for high-level protein production in mammalian cells. *Acta Crystallogr D Biol Crystallogr* 62, 1243–1250. <https://doi.org/10.1107/S0907444906029799>.
- Armando, F., Beythien, G., Kaiser, F.K., Allnoch, L., Heydemann, L., Rosiak, M., Becker, S., Gonzalez-Hernandez, M., Lamers, M.M., Haagmans, B.L., Guilfoyle, K., van Amerongen, G., Ciurkiewicz, M., Osterhaus, A.D.M.E., Baumgärtner, W., 2022. SARS-CoV-2 Omicron variant causes mild pathology in the upper and lower respiratory tract of hamsters. *Nat. Commun.* 13, 3519. <https://doi.org/10.1038/s41467-022-31200-y>.
- Chen, Y., Zhao, X., Zhou, H., Zhu, H., Jiang, S., Wang, P., 2022. Broadly neutralizing antibodies to SARS-CoV-2 and other human coronaviruses. *Nat. Rev. Immunol.* <https://doi.org/10.1038/s41577-022-00784-3>.
- Ciurkiewicz, M., Armando, F., Schreiner, T., de Buhr, N., Pilchová, V., Krupp-Buzimikic, V., Gabriel, G., von Köckritz-Blickwede, M., Baumgärtner, W., Schulz, C., Gerhauser, I., 2022. Ferrets are valuable models for SARS-CoV-2 research. *Vet. Pathol.* 59, 661–672. <https://doi.org/10.1177/03009858211071012>.
- Corman, V.M., Landt, O., Kaiser, M., Molenkamp, R., Meijer, A., Chu, D.K., Bleicker, T., Brünink, S., Schneider, J., Schmidt, M.L., Mulders, D.G., Haagmans, B.L., van der Veer, B., van den Brink, S., Wijsman, L., Goderski, G., Romette, J.L., Ellis, J., Zambon, M., Peiris, M., Goossens, H., Reusken, C., Koopmans, M.P., Drosten, C., 2020. Detection of 2019 novel coronavirus (2019-nCoV) by real-time RT-PCR. *Euro Surveill.* 25 <https://doi.org/10.2807/1560-7917.es.2020.25.3.2000045>.
- Cox, M., Peacock, T.P., Harvey, W.T., Hughes, J., Wright, D.W., Willett, B.J., Thomson, E., Gupta, R.K., Peacock, S.J., Robertson, D.L., Carabelli, A.M., Consortium, C.-G.U., 2023. SARS-CoV-2 variant evasion of monoclonal antibodies based on in vitro studies. *Nat. Rev. Microbiol.* 21, 112–124. <https://doi.org/10.1038/s41579-022-00809-7>.
- Cui, Z., Liu, P., Wang, N., Wang, L., Fan, K., Zhu, Q., Wang, K., Chen, R., Feng, R., Jia, Z., Yang, M., Xu, G., Zhu, B., Fu, W., Chu, T., Feng, L., Wang, Y., Pei, X., Yang, P., Xie, X. S., Cao, L., Cao, Y., Wang, X., 2022. Structural and functional characterizations of infectivity and immune evasion of SARS-CoV-2 Omicron. *Cell* 185, 860–871.e813. <https://doi.org/10.1016/j.cell.2022.01.019>.
- Custódio, T.F., Das, H., Sheward, D.J., Hanke, L., Pazicky, S., Pieprzyk, J., Sorgenfrei, M., Schroer, M.A., Gruzinov, A.Y., Jeffries, C.M., Graewert, M.A., Svergun, D.I., Dobrev, N., Remans, K., Seeger, M.A., McNerney, G.M., Murrell, B., Hällberg, B.M., Löw, C., 2020. Selection, biophysical and structural analysis of synthetic nanobodies that effectively neutralize SARS-CoV-2. *Nat. Commun.* 11, 5588. <https://doi.org/10.1038/s41467-020-19204-y>.
- Dolovich, M.B., Dhand, R., 2011. Aerosol drug delivery: developments in device design and clinical use. *Lancet* 377, 1032–1045. [https://doi.org/10.1016/S0140-6736\(10\)60926-9](https://doi.org/10.1016/S0140-6736(10)60926-9).
- Emsley, P., Lohkamp, B., Scott, W.G., Cowtan, K., 2010. Features and development of Coot. *Acta Crystallogr D Biol Crystallogr* 66, 486–501. <https://doi.org/10.1107/S0907444910007493>.
- Esparza, T.J., Chen, Y., Martin, N.P., Bielefeldt-Ohmann, H., Bowen, R.A., Tolbert, W.D., Paggier, M., Brody, D.L., 2022. Nebulized delivery of a broadly neutralizing SARS-CoV-2 RBD-specific nanobody prevents clinical, virological, and pathological disease in a Syrian hamster model of COVID-19. *mAbs* 14, 2047144. <https://doi.org/10.1080/19420862.2022.2047144>.
- Frey, S., Görlich, D., 2014. A new set of highly efficient, tag-cleaving proteases for purifying recombinant proteins. *J. Chromatogr. A* 1337, 95–105. <https://doi.org/10.1016/j.chroma.2014.02.029>.
- Frey, S., Rees, R., Schünemann, J., Ng, S.C., Fünfgeld, K., Huyton, T., Görlich, D., 2018. Surface properties determining passage rates of proteins through nuclear pores. *Cell* 174, 202–217.e209. <https://doi.org/10.1016/j.cell.2018.05.045>.
- Gai, J., Ma, L., Li, G., Zhu, M., Qiao, P., Li, X., Zhang, H., Zhang, Y., Chen, Y., Ji, W., Zhang, H., Cao, H., Li, X., Gong, R., Wan, Y., 2021. A potent neutralizing nanobody against SARS-CoV-2 with inhaled delivery potential. *MedComm* 2, 101–113. <https://doi.org/10.1002/mco2.60>.
- Goldberg, D.S., Bishop, S.M., Shah, A.U., Sathish, H.A., 2011. Formulation development of therapeutic monoclonal antibodies using high-throughput fluorescence and static light scattering techniques: role of conformational and colloidal stability. *J. Pharmaceut. Sci.* 100, 1306–1315. <https://doi.org/10.1002/jps.22371>.
- Güttler, T., Aksu, M., Dickmanns, A., Stegmann, K.M., Gregor, K., Rees, R., Taxer, W., Rymarenko, O., Schünemann, J., Dienemann, C., Gunkel, P., Mussil, B., Krull, J., Teichmann, U., Groß, U., Cordes, V.C., Döbelstein, M., Görlich, D., 2021. Neutralization of SARS-CoV-2 by highly potent, hyperthermostable, and mutation-tolerant nanobodies. *EMBO J.* 40, e107985 <https://doi.org/10.15252/emboj.2021107985>.
- Hamers-Casterman, C., Atarhouch, T., Muyldermans, S., Robinson, G., Hamers, C., Song, E.B., Bendahman, N., Hamers, R., 1993. Naturally occurring antibodies devoid of light chains. *Nature* 363, 446–448. <https://doi.org/10.1038/363446a0>.
- He, C., He, X., Yang, J., Lei, H., Hong, W., Song, X., Yang, L., Li, J., Wang, W., Shen, G., Lu, G., Wei, X., 2022. Spike protein of SARS-CoV-2 Omicron (B.1.1.529) variant has a reduced ability to induce the immune response. *Signal Transduct. Targeted Ther.* 7, 119. <https://doi.org/10.1038/s41392-022-00980-6>.
- Hickey, A.J., Stewart, I.E., 2022. Inhaled antibodies: quality and performance considerations. *Hum. Vaccines Immunother.* 18, 1940650 <https://doi.org/10.1080/21645515.2021.1940650>.
- Hoffmann, B., Depner, K., Schirmmeier, H., Beer, M., 2006. A universal heterologous internal control system for duplex real-time RT-PCR assays used in a detection system for pestiviruses. *J. Virol Methods* 136, 200–209. <https://doi.org/10.1016/j.jviromet.2006.05.020>.
- Hsieh, C.L., Goldsmith, J.A., Schaub, J.M., DiVenere, A.M., Kuo, H.C., Javanmardi, K., Le, K.C., Wrapp, D., Lee, A.G., Liu, Y., Chou, C.W., Byrne, P.O., Hjorth, C.K., Johnson, N.V., Ludes-Meyers, J., Nguyen, A.W., Park, J., Wang, N., Amengor, D., Lavinder, J.J., Ippolito, G.C., Maynard, J.A., Finkelstein, I.J., McLellan, J.S., 2020. Structure-based design of prefusion-stabilized SARS-CoV-2 spikes. *Science* 369, 1501–1505. <https://doi.org/10.1126/science.abc0826>.
- Huo, J., Mikolajek, H., Le Bas, A., Clark, J.J., Sharma, P., Kipar, A., Dormon, J., Norman, C., Weckener, M., Clare, D.K., Harrison, P.J., Tree, J.A., Buttigieg, K.R., Salguero, F.J., Watson, R., Knott, D., Carnell, O., Ngabo, D., Elmore, M.J., Fotheringham, S., Harding, A., Moynié, L., Ward, P.N., Dumoux, M., Prince, T., Hall, Y., Hiscoc, J.A., Owen, A., James, W., Carroll, M.W., Stewart, J.P., Naismith, J. H., Owens, R.J., 2021. A potent SARS-CoV-2 neutralising nanobody shows therapeutic efficacy in the Syrian golden hamster model of COVID-19. *Nat. Commun.* 12, 5469. <https://doi.org/10.1038/s41467-021-25480-z>.
- Huson, D.H., Scornavacca, C., 2012. Dendroscope 3: an interactive tool for rooted phylogenetic trees and networks. *Syst. Biol.* 61, 1061–1067. <https://doi.org/10.1093/sysbio/sys062>.
- Jamison, D.A., Anand Narayanan, S., Trovão, N.S., Guarnieri, J.W., Topper, M.J., Moraes-Vieira, P.M., Zaksas, V., Singh, K.K., Wurtele, E.S., Beheshti, A., 2022. A comprehensive SARS-CoV-2 and COVID-19 review. Part 1: intracellular overdrive for SARS-CoV-2 infection. *Eur. J. Hum. Genet.* 30, 889–898. <https://doi.org/10.1038/s41431-022-01108-8>.
- Jarash, A., Koll, H., Regula, J.T., Bader, M., Papadimitriou, A., Kettenberger, H., 2015. Developability assessment during the selection of novel therapeutic antibodies. *J. Pharmaceut. Sci.* 104, 1885–1898. <https://doi.org/10.1002/jps.24430>.
- Kabsch, W., 2010. XDS. *Acta Crystallogr D Biol Crystallogr* 66, 125–132. <https://doi.org/10.1107/S0907444909047337>.
- Kärber, G., 1931. Beitrag zur kollektiven Behandlung pharmakologischer Reihenversuche. *Schmiedeb. Arch. für Exp. Pathol. Pharmacol.* 162, 480–483. <https://doi.org/10.1007/BF01863914>.
- Kiener, M., Roldan, N., Machahua, C., Sengupta, A., Geiser, T., Guenat, O.T., Funke-Chambour, M., Hobi, N., Kruithof-de Julio, M., 2021. Human-based advanced in vitro approaches to investigate lung fibrosis and pulmonary effects of COVID-19. *Front. Med.* 8 <https://doi.org/10.3389/fmed.2021.644678>.
- Koenig, P.A., Das, H., Liu, H., Kümmerer, B.M., Gohr, F.N., Jenster, L.M., Schiffelers, L.D. J., Tesfamariam, Y.M., Uchima, M., Wuerth, J.D., Gatterdam, K., Ruetalo, N., Christensen, M.H., Fandrey, C.I., Normann, S., Todtmann, J.M.P., Pritzl, S., Hanke, L., Boos, J., Yuan, M., Zhu, X., Schmid-Burgk, J.L., Kato, H., Schindler, M., Wilson, I.A., Geyer, M., Ludwig, K.U., Hallberg, B.M., Wu, N.C., Schmidt, F.I., 2021a. Structure-guided multivalent nanobodies block SARS-CoV-2 infection and suppress mutational escape. *Science* 371. <https://doi.org/10.1126/science.abe6230>.
- Koenig, P.A., Das, H., Liu, H., Kümmerer, B.M., Gohr, F.N., Jenster, L.M., Schiffelers, L.D. J., Tesfamariam, Y.M., Uchima, M., Wuerth, J.D., Gatterdam, K., Ruetalo, N., Christensen, M.H., Fandrey, C.I., Normann, S., Todtmann, J.M.P., Pritzl, S., Hanke, L., Boos, J., Yuan, M., Zhu, X., Schmid-Burgk, J.L., Kato, H., Schindler, M., Wilson, I.A., Geyer, M., Ludwig, K.U., Hallberg, B.M., Wu, N.C., Schmidt, F.I., 2021b. Structure-guided multivalent nanobodies block SARS-CoV-2 infection and suppress mutational escape. *Science* 371. <https://doi.org/10.1126/science.abe6230>.
- Koide, S., Sidhu, S.S., 2009. The importance of being tyrosine: lessons in molecular recognition from minimalist synthetic binding proteins. *ACS Chem. Biol.* 4, 325–334. <https://doi.org/10.1021/cb800314v>.
- Li, W., Moore, M.J., Vasilieva, N., Sui, J., Wong, S.K., Berne, M.A., Somasundaran, M., Sullivan, J.L., Luzuriaga, K., Greenough, T.C., Choe, H., Farzan, M., 2003. Angiotensin-converting enzyme 2 is a functional receptor for the SARS coronavirus. *Nature* 426, 450–454. <https://doi.org/10.1038/nature02145>.

- Liebschner, D., Afonine, P.V., Baker, M.L., Bunkóczi, G., Chen, V.B., Croll, T.I., Hintze, B., Hung, L.W., Jain, S., McCoy, A.J., Moriarty, N.W., Oeffner, R.D., Poon, B.K., Prisant, M.G., Read, R.J., Richardson, J.S., Richardson, D.C., Sammito, M.D., Sobolev, O.V., Stockwell, D.H., Terwilliger, T.C., Urzhumtsev, A.G., Videau, L.L., Williams, C.J., Adams, P.D., 2019. Macromolecular structure determination using X-rays, neutrons and electrons: recent developments in Phenix. *Acta Crystallogr D Struct Biol* 75, 861–877. <https://doi.org/10.1107/s2059798319011471>.
- Longest, W., Spence, B., Hindle, M., 2019. Devices for improved delivery of nebulized pharmaceutical aerosols to the lungs. *J. Aerosol Med. Pulm. Drug Deliv.* 32, 317–339. <https://doi.org/10.1089/jamp.2018.1508>.
- Maeda, R., Fujita, J., Konishi, Y., Kazuma, Y., Yamazaki, H., Anzai, I., Watanabe, T., Yamaguchi, K., Kasai, K., Nagata, K., Yamaoka, Y., Miyakawa, K., Ryo, A., Shirakawa, K., Sato, K., Makino, F., Matsuura, Y., Inoue, T., Imura, A., Namba, K., Takaori-Kondo, A., 2022. A panel of nanobodies recognizing conserved hidden clefts of all SARS-CoV-2 spike variants including Omicron. *Commun. Biol.* 5, 669. <https://doi.org/10.1038/s42003-022-03630-3>.
- Mast, F.D., Fridy, P.C., Ketaren, N.E., Wang, J., Jacobs, E.Y., Olivier, J.P., Sanyal, T., Molloy, K.R., Schmidt, F., Rutkowska, M., Weisblum, Y., Rich, L.M., Vanderwall, E. R., Dambrauskas, N., Vigdorovich, V., Keegan, S., Jiler, J.B., Stein, M.E., Olinares, P. D.B., Herlands, L., Hatzioannou, T., Sather, D.N., Debley, J.S., Fenyö, D., Sali, A., Bieniasz, P.D., Aitchison, J.D., Chait, B.T., Rout, M.P., 2021. Highly synergistic combinations of nanobodies that target SARS-CoV-2 and are resistant to escape. *Elife* 10. <https://doi.org/10.7554/eLife.73027>.
- Mastronarde, D.N., 2005. Automated electron microscopy tomography using robust prediction of specimen movements. *J. Struct. Biol.* 152, 36–51. <https://doi.org/10.1016/j.jsb.2005.07.007>.
- Mayor, A., Thibert, B., Huille, S., Respaud, R., Audat, H., Heuzé-Vourc'h, N., 2021. Inhaled antibodies: formulations require specific development to overcome instability due to nebulization. *Drug Deliv. Transl. Res.* 11, 1625–1633. <https://doi.org/10.1007/s13346-021-00967-w>.
- McCoy, A.J., 2007. Solving structures of protein complexes by molecular replacement with Phaser. *Acta Crystallogr D Biol. Crystallogr.* 63, 32–41. <https://doi.org/10.1107/s0907444906045975>.
- Mergulhão, F.J., Summers, D.K., Monteiro, G.A., 2005. Recombinant protein secretion in *Escherichia coli*. *Biotechnol. Adv.* 23, 177–202. <https://doi.org/10.1016/j.biotechadv.2004.11.003>.
- Meyer zu Natrup, C., Tschernae, A., Dahlke, C., Ciurkiewicz, M., Shin, D.-L., Fathi, A., Rohde, C., Kalodimos, G., Halwe, S., Limpinsel, L., Schwarz, J.H., Klug, M., Esen, M., Schneiderhan-Marra, N., Dulovic, A., Kupke, A., Brosinski, K., Clever, S., Schünemann, L.-M., Beythien, G., Armando, F., Mayer, L., Weskamm, M.L., Jany, S., Freudenstein, A., Tüchel, T., Baumgärtner, W., Kremsner, P., Fendel, R., Addo, M.M., Becker, S., Sutter, G., Volz, A., 2022. Stabilized recombinant SARS-CoV-2 spike antigen enhances vaccine immunogenicity and protective capacity. *J. Clin. Invest.* 132. <https://doi.org/10.1172/JCI159895>.
- Meyerholz, D.K., Sieren, J.C., Beck, A.P., Flaherty, H.A., 2018. Approaches to evaluate lung inflammation in translational research. *Vet. Pathol.* 55, 42–52. <https://doi.org/10.1177/0300985817726117>.
- Motulsky, H.-J., Brown, R.E., 2006. Detecting outliers when fitting data with nonlinear regression - a new method based on robust nonlinear regression and the false discovery rate. *BMC Bioinf.* 7, 123. <https://doi.org/10.1186/1471-2105-7-123>.
- Moulana, A., Dupic, T., Phillips, A.M., Chang, J., Roffler, A.A., Greaney, A.J., Starr, T.N., Bloom, J.D., Desai, M.M., 2023. The landscape of antibody binding affinity in SARS-CoV-2 Omicron BA.1 evolution. *Elife* 12, e83442. <https://doi.org/10.7554/eLife.83442>.
- Murakami, N., Hayden, R., Hills, T., Al-Samkari, H., Casey, J., Del Sorbo, L., Lawler, P.R., Sise, M.E., Leaf, D.E., 2023. Therapeutic advances in COVID-19. *Nat. Rev. Nephrol.* 19, 38–52. <https://doi.org/10.1038/s41581-022-00642-4>.
- Nambulli, S., Xiang, Y., Tilston-Lunel, N.L., Rennick, L.J., Sang, Z., Klimstra, W.B., Reed, D.S., Crossland, N.A., Shi, Y., Duprex, W.P., 2021. Inhalable Nanobody (PiN-21) prevents and treats SARS-CoV-2 infections in Syrian hamsters at ultra-low doses. *Sci. Adv.* 7. <https://doi.org/10.1126/sciadv.abh0319>.
- Petersen, E.F., Goddard, T.D., Huang, C.C., Couch, G.S., Greenblatt, D.M., Meng, E.C., Ferrin, T.E., 2004. UCSF Chimera—a visualization system for exploratory research and analysis. *J. Comput. Chem.* 25, 1605–1612. <https://doi.org/10.1002/jcc.20084>.
- Piepenbrink, M.S., Park, J.-G., Oladunni, F.S., Deshpande, A., Basu, M., Sarkar, S., Loos, A., Woo, J., Lovalenti, P., Sloan, D., Ye, C., Chiemi, K., Bates, C.W., Burch, R.E., Erdmann, N.B., Goepfert, P.A., Truong, V.L., Walter, M.R., Martinez-Sobrido, L., Kobia, J.J., 2021. Therapeutic activity of an inhaled potent SARS-CoV-2 neutralizing human monoclonal antibody in hamsters. *Cell Rep. Med.* 2, 100218. <https://doi.org/10.1016/j.xcrm.2021.100218>.
- Pleiner, T., Bates, M., Trakhanov, S., Lee, C.T., Schliep, J.E., Chug, H., Böhning, M., Stark, H., Uralbach, H., Görlisch, D., 2015. Nanobodies: site-specific labeling for super-resolution imaging, rapid epitope-mapping and native protein complex isolation. *Elife* 4, e11349. <https://doi.org/10.7554/eLife.11349>.
- Pohlmann, G., Hohlfield, J.M., Haidl, P., Pankalla, J., Cloes, R.M., 2018. Assessment of the power required for optimal use of current inhalation devices. *J. Aerosol Med. Pulm. Drug Deliv.* 31, 339–346. <https://doi.org/10.1089/jamp.2017.1376>.
- Pym, P., Adair, A., Chan, L.-J., Cooney, J.P., Mordant, F.L., Allison, C.C., Lopez, E., Haycroft, E.R., O'Neill, M.T., Tan, L.L., Dietrich, M.H., Drew, D., Doerflinger, M., Dengler, M.A., Scott, N.E., Wheatley, A.K., Gherardin, N.A., Venugopal, H., Cromer, D., Davenport, M.P., Pickering, R., Godfrey, D.I., Purcell, D.F.J., Kent, S.J., Chung, A.W., Subbarao, K., Pellegrini, M., Glukhova, A., Tham, W.-H., 2021. Nanobody cocktails potentially neutralize SARS-CoV-2 D614G N501Y variant and protect mice. *Proc. Natl. Acad. Sci. USA* 118, e2101918118. <https://doi.org/10.1073/pnas.2101918118>.
- Rossotti, M.A., van Faassen, H., Tran, A.T., Sheff, J., Sandhu, J.K., Duque, D., Hewitt, M., Wen, X., Bavananthasivam, J., Beitari, S., Matte, K., Laroche, G., Giguère, P.M., Gervais, C., Stuble, M., Guimond, J., Perret, S., Hussack, G., Langlois, M.-A., Durocher, Y., Tanha, J., 2022. Arsenal of nanobodies shows broad-spectrum neutralization against SARS-CoV-2 variants of concern in vitro and in vivo in hamster models. *Commun. Biol.* 5, 933. <https://doi.org/10.1038/s42003-022-03866-z>.
- Sasisekharan, R., 2021. Preparing for the future — nanobodies for covid-19? *N. Engl. J. Med.* 384, 1568–1571. <https://doi.org/10.1056/NEJMcibr2101205>.
- Schulz, C., Wylezich, C., Wernike, K., Gründl, M., Dangel, A., Baechlein, C., Hoffmann, D., Röhrs, S., Hepner, S., Ackermann, N., Sing, A., Pink, I., Länger, B., Volk, H.A., Becher, P., Sutter, G., Neubauer-Juric, A., von Köckritz-Blickwede, M., Beer, M., Volz, A., 2021. Prolonged SARS-CoV-2 RNA shedding from therapy cat after cluster outbreak in retirement home. *Emerg. Infect. Dis.* 27, 1974–1976. <https://doi.org/10.3201/eid2707.204670>.
- Sievers, F., Wilm, A., Dineen, D., Gibson, T.J., Karplus, K., Li, W., Lopez, R., McWilliam, H., Remmert, M., Söding, J., Thompson, J.D., Higgins, D.G., 2011. Fast, scalable generation of high-quality protein multiple sequence alignments using Clustal Omega. *Mol. Syst. Biol.* 7, 539. <https://doi.org/10.1038/msb.2011.75>.
- Smither, S.J., Lear-Rooney, C., Biggins, J., Pettitt, J., Lever, M.S., Olinger, G.G., 2013. Comparison of the plaque assay and 50% tissue culture infectious dose assay as methods for measuring filovirus infectivity. *J. Virol. Methods* 193, 565–571. <https://doi.org/10.1016/j.jviromet.2013.05.015>.
- Stegmann, K.M., Dickmanns, A., Gerber, S., Nikolova, V., Klemke, L., Manzini, V., Schüssler, D., Bierwirth, C., Freund, J., Sitt, M., Lugert, R., Salinas, G., Meister, T.L., Pfander, S., Görlisch, D., Wollnik, B., Groß, U., Döbelstein, M., 2021. The folate antagonist methotrexate diminishes replication of the coronavirus SARS-CoV-2 and enhances the antiviral efficacy of remdesivir in cell culture models. *Virus Res.* 302, 198469. <https://doi.org/10.1016/j.virusres.2021.198469>.
- Tegunov, D., Cramer, P., 2019. Real-time cryo-electron microscopy data preprocessing with Warp. *Nat. Methods* 16, 1146–1152. <https://doi.org/10.1038/s41592-019-0580-y>.
- Terwilliger, T.C., Grosse-Kunstleve, R.W., Afonine, P.V., Moriarty, N.W., Zwart, P.H., Hung, L.W., Read, R.J., Adams, P.D., 2008. Iterative model building, structure refinement and density modification with the PHENIX AutoBuild wizard. *Acta Crystallogr D Biol. Crystallogr.* 64, 61–69. <https://doi.org/10.1107/s090744490705024x>.
- Tuekprakhon, A., Nutalai, R., Dijkaita-Guraliuc, A., Zhou, D., Ginn, H.M., Selvaraj, M., Liu, C., Mentzer, A.J., Supasa, P., Duyvesteyn, H.M.E., Das, R., Skelly, D., Ritter, T. G., Amini, A., Bibi, S., Adele, S., Johnson, S.A., Constantinides, B., Webster, H., Temperton, N., Klennerman, P., Barnes, E., Dunachie, S.J., Crook, D., Pollard, A.J., Lambe, T., Goulder, P., Paterson, N.G., Williams, M.A., Hall, D.R., Fry, E.E., Huo, J., Mongkolsapaya, J., Ren, J., Stuart, D.I., Screaton, G.R., 2022. Antibody escape of SARS-CoV-2 Omicron BA.4 and BA.5 from vaccine and BA.1 serum. *Cell* 185, 2422–2433.e2413. <https://doi.org/10.1016/j.cell.2022.06.005>.
- Van Heeke, G., Allosery, K., De Brabandere, V., De Smedt, T., Detalle, L., de Fougères, A., 2017. Nanobodies® as inhaled biotherapeutics for lung diseases. *Pharmacol. Ther.* 169, 47–56. <https://doi.org/10.1016/j.pharmthera.2016.06.012>.
- VanBlargan, L.A., Errico, J.M., Halfmann, P.J., Zost, S.J., Crowe, J.E., Purcell, L.A., Kawaoka, Y., Corti, D., Fremont, D.H., Diamond, M.S., 2022. An infectious SARS-CoV-2 B.1.1.529 Omicron virus escapes neutralization by therapeutic monoclonal antibodies. *Nat. Med.* 28, 490–495. <https://doi.org/10.1038/s41591-021-01678-y>.
- Waterhouse, A., Bertoni, M., Bienert, S., Studer, G., Tauriello, G., Gumienny, R., Heer, F. T., de Beer, T.A.P., Rempe, C., Bordoli, L., Lepore, R., Schwede, T., 2018. SWISS-MODEL: homology modelling of protein structures and complexes. *Nucleic Acids Res.* 46, W296–w303. <https://doi.org/10.1093/nar/gky427>.
- Williams, C.J., Headd, J.J., Moriarty, N.W., Prisant, M.G., Videau, L.L., Deis, L.N., Verma, V., Keedy, D.A., Hintze, B.J., Chen, V.B., Jain, S., Lewis, S.M., Arendall 3rd, W.B., Snoeyink, J., Adams, P.D., Lovell, S.C., Richardson, J.S., Richardson, D.C., 2018. MolProbity: more and better reference data for improved all-atom structure validation. *Protein Sci.* 27, 293–315. <https://doi.org/10.1002/pro.3330>.
- Wu, S., Letchworth, G.J., 2004. High efficiency transformation by electroporation of *Pichia pastoris* pretreated with lithium acetate and dithiothreitol. *Biotechniques* 36, 152–154. <https://doi.org/10.2144/04361402>.
- Wu, X., Wang, Y., Cheng, L., Ni, F., Zhu, L., Ma, S., Huang, B., Ji, M., Hu, H., Li, Y., Xu, S., Shi, H., Zhang, D., Liu, L., Nawaz, W., Hu, Q., Ye, S., Liu, Y., Wu, Z., 2022. Short-term instantaneous prophylaxis and efficient treatment against SARS-CoV-2 in hACE2 mice conferred by an intranasal nanobody (Nb22). *Front. Immunol.* 13, 865401. <https://doi.org/10.3389/fimmu.2022.865401>.
- Xiang, Y., Huang, W., Liu, H., Sang, Z., Nambulli, S., Tubiana, J., Williams Jr., K.L., Duprex, W.P., Schneidman-Duhovny, D., Wilson, I.A., Taylor, D.J., Shi, Y., 2022. Superimmunity by pan-sarbecovirus nanobodies. *Cell Rep.* 39, 111004. <https://doi.org/10.1016/j.celrep.2022.111004>.
- Xiang, Y., Nambulli, S., Xiao, Z., Liu, H., Sang, Z., Duprex, W.P., Schneidman-Duhovny, D., Zhang, C., Shi, Y., 2020. Versatile and multivalent nanobodies efficiently neutralize SARS-CoV-2. *Science* 370, 1479–1484. <https://doi.org/10.1126/science.abe4747>.
- Xu, J., Xu, K., Jung, S., Conte, A., Lieberman, J., Muecksch, F., Lorenzi, J.C.C., Park, S., Schmidt, F., Wang, Z., Huang, Y., Luo, Y., Nair, M.S., Wang, P., Schulz, J.E., Tessarollo, L., Bylund, T., Chuang, G.-Y., O'Neil, A.S., Stephens, T., Teng, I.T., Tsybovsky, Y., Zhou, T., Munster, V., Ho, D.D., Hatzioannou, T., Bieniasz, P.D., Nussenzweig, M.C., Kwong, P.D., Casellas, R., 2021. Nanobodies from camelid mice and llamas neutralize SARS-CoV-2 variants. *Nature* 595, 278–282. <https://doi.org/10.1038/s41586-021-03676-z>.

- Ye, G., Gallant, J., Zheng, J., Massey, C., Shi, K., Tai, W., Odle, A., Vickers, M., Shang, J., Wan, Y., Du, L., Aihara, H., Perlman, S., LeBeau, A., Li, F., 2021. The development of Nanosota-1 as anti-SARS-CoV-2 nanobody drug candidates. *Elife* 10, e64815. <https://doi.org/10.7554/eLife.64815>.
- Zhang, L., Narayanan, K.K., Cooper, L., Chan, K.K., Skeeters, S.S., Devlin, C.A., Aguhob, A., Shirley, K., Rong, L., Rehman, J., Malik, A.B., Procko, E., 2022. An ACE2 decoy can be administered by inhalation and potently targets omicron variants of SARS-CoV-2. *EMBO Mol. Med.* 14, e16109 <https://doi.org/10.15252/emmm.202216109>.
- Zhang, Y., Huo, M., Zhou, J., Xie, S., 2010. PKSolver: an add-in program for pharmacokinetic and pharmacodynamic data analysis in Microsoft Excel. *Comput. Methods Progr. Biomed.* 99, 306–314. <https://doi.org/10.1016/j.cmpb.2010.01.007>.
- Zhou, T., Tsybovsky, Y., Gorman, J., Rapp, M., Cerutti, G., Chuang, G.Y., Katsamba, P.S., Sampson, J.M., Schön, A., Bimela, J., Boyington, J.C., Nazzari, A., Olla, A.S., Shi, W., Sastry, M., Stephens, T., Stuckey, J., Teng, I.T., Wang, P., Wang, S., Zhang, B., Friesner, R.A., Ho, D.D., Mascola, J.R., Shapiro, L., Kwong, P.D., 2020. Cryo-EM structures of SARS-CoV-2 spike without and with ACE2 reveal a pH-dependent switch to mediate endosomal positioning of receptor-binding domains. *Cell Host Microbe* 28, 867–879.e865. <https://doi.org/10.1016/j.chom.2020.11.004>.
- Zibat, A., Zhang, X., Dickmanns, A., Stegmann, K.M., Döbelstein, A.W., Alachram, H., Soliwoda, R., Salinas, G., Groß, U., Görlich, D., Kschischo, M., Wollnik, B., Döbelstein, M., 2023. N4-hydroxycytidine, the active compound of Molnupiravir, promotes SARS-CoV-2 mutagenesis and escape from a neutralizing nanobody. *iScience* 26, 107786. <https://doi.org/10.1016/j.isci.2023.107786>.
- Zimmer, G., Locher, S., Berger Rentsch, M., Halbherr, S.J., 2014. Pseudotyping of vesicular stomatitis virus with the envelope glycoproteins of highly pathogenic avian influenza viruses. *J. Gen. Virol.* 95, 1634–1639. <https://doi.org/10.1099/vir.0.065201-0>.
- Zivanov, J., Nakane, T., Forsberg, B.O., Kimanius, D., Hagen, W.J., Lindahl, E., Scheres, S.H., 2018. New tools for automated high-resolution cryo-EM structure determination in RELION-3. *eLife* 7. <https://doi.org/10.7554/eLife.42166>.